

Spring 2003

Vertical polymer tunneling sensor platform by hot embossing technique

Jing Wang

Follow this and additional works at: <https://digitalcommons.latech.edu/dissertations>

Recommended Citation

Wang, Jing, "" (2003). *Dissertation*. 650.
<https://digitalcommons.latech.edu/dissertations/650>

This Dissertation is brought to you for free and open access by the Graduate School at Louisiana Tech Digital Commons. It has been accepted for inclusion in Doctoral Dissertations by an authorized administrator of Louisiana Tech Digital Commons. For more information, please contact digitalcommons@latech.edu.

INFORMATION TO USERS

This manuscript has been reproduced from the microfilm master. UMI films the text directly from the original or copy submitted. Thus, some thesis and dissertation copies are in typewriter face, while others may be from any type of computer printer.

The quality of this reproduction is dependent upon the quality of the copy submitted. Broken or indistinct print, colored or poor quality illustrations and photographs, print bleedthrough, substandard margins, and improper alignment can adversely affect reproduction.

In the unlikely event that the author did not send UMI a complete manuscript and there are missing pages, these will be noted. Also, if unauthorized copyright material had to be removed, a note will indicate the deletion.

Oversize materials (e.g., maps, drawings, charts) are reproduced by sectioning the original, beginning at the upper left-hand corner and continuing from left to right in equal sections with small overlaps.

ProQuest Information and Learning
300 North Zeeb Road, Ann Arbor, MI 48106-1346 USA
800-521-0600

UMI[®]

**VERTICAL POLYMER TUNNELING SENSOR
PLATFORM BY HOT EMBOSSING
TECHNIQUE**

by

Jing Wang, B.S. and M.S.

**A Dissertation Presented in Partial Fulfillment
of the Requirements for the Degree
Ph.D. in Engineering**

**COLLEGE OF ENGINEERING AND SCIENCE
LOUISIANA TECH UNIVERSITY**

May 2003

UMI Number: 3084546

UMI[®]

UMI Microform 3084546

Copyright 2003 by ProQuest Information and Learning Company.

All rights reserved. This microform edition is protected against
unauthorized copying under Title 17, United States Code.

ProQuest Information and Learning Company

300 North Zeeb Road

P.O. Box 1346

Ann Arbor, MI 48106-1346

LOUISIANA TECH UNIVERSITY

THE GRADUATE SCHOOL

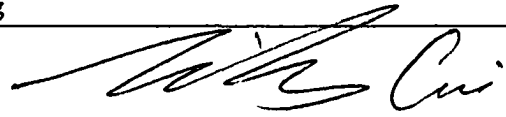
04/24/2003

Date

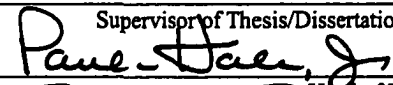
We hereby recommend that the thesis/dissertation prepared under our supervision
by Jing Wang

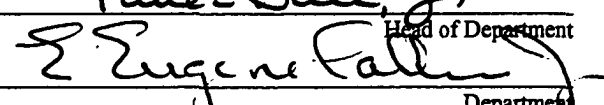
entitled Vertical Polymer Tunneling Sensor Platform by Hot
Embossing Technique

be accepted in partial fulfillment of the requirements for the Degree of
Ph.D. in Engineering

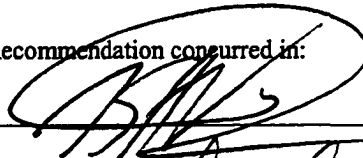



Supervisor of Thesis/Dissertation Research




Head of Department


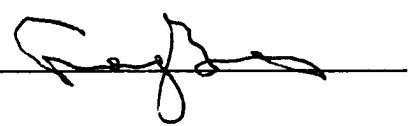
Department

Recommendation concurred in:






Advisory Committee



Approved:


Director of Graduate Studies

Approved:


Dean of the Graduate School



Dean of the College

ABSTRACT

Recent development in microfabrication technology has brought much attention to the development of miniaturized, inexpensive and high-accuracy MEMS devices and microsystems. The ultimate goal of our project is to develop a versatile, three-dimensional, high precision sensor platform, which can be used for displacement, velocity or acceleration measurement. The first step, on which this dissertation is based, is to fabricate a one-dimensional (parallel with the Z axis) tunneling sensor, which in turn can be developed into two- and three-dimensional sensor platforms through structural and functional integration.

Since the invention of mini-structured high-sensitivity silicon-based tunneling sensor in 1993, the synthesis and fabrication of PMMA-based tunneling sensors still remains an over-looked area. Compared with traditional silicon-based tunneling sensors, PMMA is less expensive, has little stiffness, and is easier to work with micro-machining process. Moreover, this all-PMMA-based tunneling sensor is one of the first generations of functional micro-sensors/devices for organic compatible applications.

The hot embossing technique, one of the most widely used micromachining approaches in “soft-lithography”, was chosen for its fast turnaround, fewer processing parameters, and simplicity. Because the mold can be used repeatedly, the potential of mass-production is further highlighted in this dissertation. ●

All-PMMA-based tunneling vertical sensors have been successfully fabricated. The overall size of the packaged sensor is 8 mm × 8 mm × 1 mm, with the measurement circuits bounded together. The natural frequency of the sensor structure is 133 Hz. The bandwidth of the feedback system is 6.3 kHz with voltage over acceleration sensitivity of 20.6 V/g. The resolution at 192 Hz is $0.2485 \mu\text{g} / \sqrt{\text{Hz}}$.

Compared with the silicon-based tunneling sensor, the PMMA sensor's apparent advantages are: low cost, less processing time, less processing instruments, high yields, wider bandwidth, and theoretically lower noise level. Given all our research results, we can expect that the PMMA-based tunneling sensor platform to become the base for the next generation of highly sensitive micro-sensors in many important areas, notably in chemical, magnetic, infrared, and organic applications.

APPROVAL FOR SCHOLARLY DISSEMINATION

The author grants to the Prescott Memorial Library of Louisiana Tech University the right to reproduce, by appropriate methods, upon request, any or all portions of this Thesis. It is understood that "proper request" consists of the agreement, on the part of the requesting party, that said reproduction is for his personal use and that subsequent reproduction will not occur without written approval of the author of this Thesis. Further, any portions of the Thesis used in books, papers, and other works must be appropriately referenced to this Thesis.

Finally, the author of this dissertation reserves the right to publish freely, in the literature, at any time, any or all portions of this Thesis.

Author Wang Fj
Date 5/15/03

TABLE OF CONTENTS

CHAPTER 1	INTRODUCTION TO RESEARCH	1
1.1	Research Review.....	1
1.2	Objective	2
1.3	Methodology	4
1.4	Process Instruments and Measurement System	5
1.4.1	Photolithography and Clean Room.....	5
1.4.2	Hot Embossing.....	9
1.4.3	Measurement System.....	14
CHAPTER 2	STRUCTURE DESIGN AND SIMULATION.....	19
2.1	Design Methodology.....	19
2.2	Design of Manufacturing	19
2.3	Proof mass and Mechanical Simulation by ANSYS	22
2.3.1	Introduction to ANSYS.....	22
2.3.2	Static Analysis	23
2.3.3	Model Analysis	26
2.3.4	Harmonic Response	29
2.3.5	Static Force and Bending.....	31
2.3.6	Parameter Design Based on ANSYS	32
2.4	Electronic Control and Feedback Circuit.....	33
CHAPTER 3	MODELING AND CONTROL SYSTEM SYNTHESIS BY MATLAB	37
3.1	Introduction.....	37
3.2	Accelerometer Structure	39
3.3	Modeling	39
3.4	Small Input Analysis.....	42
3.5	Feedback and Control Design	43
3.6	Simulation Results and Discussions	47
3.6.1	Closed loop system evaluation.....	47
3.6.2	Tunneling Accelerometer Function Simulation.....	49
3.7	Summaries.....	52
CHAPTER 4	FABRICATION AND PROCESSES.....	53
4.1	PMMA Material Properties.....	53
4.2	Fabrication of Mold	56
4.2.1	Photolithography.....	56

4.2.2	BOE Etching	58
4.2.3	KOH Anisotropic Etching.....	61
4.3	Hot Embossed Sensor Structure.....	66
4.3.1	Introduction About Hot Embossing	67
4.3.2	Parameters and Properties.....	70
4.4	Assembling and Packaging	75
4.4.1	Electrode Pattern	75
4.4.2	Package	77
CHAPTER 5 MEASUREMENTs AND DISCUSSIONS.....		79
5.1	Function Frame of Measurement System	79
5.2	Resonance of Proof Mass.....	80
5.3	Open Loop Measurement.....	81
5.3.1	Electrode Deflection Rule.....	83
5.3.2	Tunneling Current Verification.....	84
5.4	Closed loop Responses	85
5.4.1	Sensitivity	85
5.4.2	Frequency Response	86
5.5	Resolution Measurement	87
5.5.1	Noise	87
5.5.2	Time History Record.....	89
5.5.3	Noise Level Resolution.....	90
CHAPTER 6 CONCLUSION AND FUTURE WORK		92
6.1	Conclusion	92
6.1.1	Structure Simulation by ANSYS	92
6.1.2	Feedback and Control System Synthesis by MatLab	93
6.1.3	Combination Technique to Fabricate Silicon Mold for Hot Embossing.....	94
6.1.4	All-PMMA Vertical Membrane Tunneling Structure Fabrication	94
6.1.5	Tunneling Effect Measurement and Evaluation	94
6.1.6	Comparison with silicon-based tunneling sensor	95
6.2	Future Work	95
6.2.1	Three-dimensional Accelerometer.....	95
6.2.2	PMMA IR Sensor	96
6.2.3	Chemical Sensor	96
6.2.4	Magnetic Sensor.....	96
Reference	97

LIST OF TABLES

Table 1-1. Optimized Conditions for PR1813	6
Table 1-2. Optimized Conditions for NR9 stripping	8
Table 2-1. Structure Parameter with Simulated <i>K</i> Values	24
Table 2-2. Electrostatic Deflection Summary.....	31
Table 2-3. Parameter List of Different proof Mass Sheet.....	34
Table 4-1. PMMA (Polymethyl methacrylate) at A Glance	55
Table 4-2. Hot Embossing Commands and Explanation.....	73
Table 6-1. Brief comparison of PMMA- to silicon- based tunneling sensor.....	95

LIST OF FIGURES

Figure 1-1 Cross-section schematic of a micromachined tunneling sensor.....	2
Figure 1-2 Process of hot embossing.....	10
Figure 1-3 Thermo-mechanical behavior of material	11
Figure 1-4 Function illustration of measurement.....	13
Figure 1-5 Scheme of the PC-based digital vibrometer system VDD 650	15
Figure 1-6 Portable PULSE measurement system.....	16
Figure 2-1 Design flowchart	20
Figure 2-2 Cross section of vertical tunneling accelerometer	21
Figure 2-3 Processing flow chart for PMMA tunneling sensor	21
Figure 2-4 Structure schematic and loading conditions at static analysis	25
Figure 2-5 Spring constant versus proof mass size at different sheet parameters	25
Figure 2-6 First vibration model simulated by AnSys.....	26
Figure 2-7 Second vibration model simulated by AnSys	27
Figure 2-8 Twist as third vibration model by AnSys.....	28
Figure 2-9 Fluctuation as the fourth vibration model by AnSys	28
Figure 2-10 Displacement response vs. frequency	29
Figure 2-11 Displacement contour plot at 1 <i>mg</i> acceleration	30
Figure 2-12 Deformation when 50 V applied on to actuator	32
Figure 2-13 Static force distribution produced by actuator	33

Figure 2-14 Feedback and control circuit for accelerometer	35
Figure 3-1 Cross section schematic of micromachined tunneling accelerometer.....	38
Figure 3-2 MatLab Simulink Modeling Block diagram	40
Figure 3-3 Normalized closed loop transfer function H'	44
Figure 3-4 Step response of normalized closed loop system	45
Figure 3-5 Bode diagram of synthesized control system.....	45
Figure 3-6 Gain Margin and Phase Margin illustration for control System	46
Figure 3-7 Illustration of root locus concept.....	47
Figure 3-8 Root locus of closed loop system.....	48
Figure 3-9 Transfer function of the tunneling accelerometer	49
Figure 3-10 Time history of output voltage	50
Figure 3-11 Tunneling current vs deflection voltage.....	51
Figure 3-12 System sensitivity frequency responses.....	51
Figure 4-1 PMMA molecule and its rotation.....	54
Figure 4-2 PMMA molecular structure.....	54
Figure 4-3 Patterned wafer by negative photolithography	58
Figure 4-4 BOE etching of SiO_2	61
Figure 4-5 KOH etching process	63
Figure 4-6 Cross section view of mold sidewall.....	64
Figure 4-7 Top view of silicon window etched by hot KOH	64
Figure 4-8 Top view of pyramid pit after hot KOH etching.....	65
Figure 4-9 SEM plot of silicon mold made by hot KOH anisotropic etching	65

Figure 4-10 Hot Embossing illustration.....	67
Figure 4-11 Hot embossing master	68
Figure 4-12 Photograph of embossed PMMA	68
Figure 4-13 Top part of hot embossing machine	69
Figure 4-14 Bottom part of hot embossing machine	69
Figure 4-15 Schematic of demolding procedure.....	72
Figure 4-16 Flowchart of the hot embossing process	72
Figure 4-17 Hot Embossing machine overview.....	74
Figure 4-18 SEM plot of sensor right after hot embossing.....	74
Figure 4-19 Close-up of tunneling tip made by hot embossing.....	75
Figure 4-20 Photograph of patterned electrode	75
Figure 4-21 Close-up of electrodes.....	76
Figure 4-22 Packaged PMMA tunneling sensors	77
Figure 5-1 Function frames for measurement.....	79
Figure 5-2 Resonant frequency measurement.....	80
Figure 5-3 Measurement of natural frequency.....	81
Figure 5-4 Open loop measurement.....	82
Figure 5-5 Tunneling current changes depend on deflection voltage	82
Figure 5-6 Actuator deflection rule measurement	83
Figure 5-7 Deflection rule measurement	83
Figure 5-8 Tunneling relation between current and displacement.....	84
Figure 5-9 Sensitivity measurement of PMMA accelerometer	85

Figure 5-10 Bandwidth measurement of PMMA sensor 86

Figure 5-11 Elementary thermal Noise Generator..... 87

Figure 5-12 Noise measurement 89

Figure 5-13 Time history record for 15 seconds..... 90

Figure 5-14 Noise spectrum of PMMA tunneling sensor 91

ACKNOWLEDGMENTS

I would firstly acknowledge the care and help from Dr. Tianhong Cui during my Ph.D. study at Institute for Micromanufacturing, Louisiana Tech University. I have learned much from Dr. Cui because of his cautious, conscientious, and strict pursuit toward science and research. Dr. Cui not only directed me with the most zealous instructions on research and study, but also presented to me intense solicitudes on daily living. Moreover, Dr. Cui brought forward many precious ideas and opinions on my dissertation at the endgame, which will be engraved on my heart whenever and wherever I am.

I would then thank the group members for their unselfish cooperation with good faith, especially to Mr. Yongjun Zhao and Mr. Wei Xue; their pure-hearted assistance and aid deserve my earnest appreciation.

I would also thank all the supporting staff at the Institute for Micromanufacturing. From Mr. Ji Fang, I could always find the earnest advice when I needed; from Dr. Karen Xu, I could obtain the first-aid when I asked; from Mr. Dee Tatum, I could always get the most prompt support; and from Mr. John McDonald, I received care for all the instruments and chemicals.

Finally, I would give my thanks to all the other committee members, Dr. Kody Varahramyan, Dr. Louis Roemer, Dr. Frank Ji, and Mr. Fang. I wish them all a wonderful life and promising future.

CHAPTER 1

INTRODUCTION TO RESEARCH

1.1 Research Review

The interdisciplinary use of lithographic, micromachining, and other micro fabrication technologies to prepare miniaturized, reliable, and inexpensive sensors, actuators, and circuit components has made tremendous breakthroughs in numerous modern fields such as mechanical [1], optical [2], thermal [3], chemical [4], biological [5], fluidic [6], and magnetic [7] technologies. Since the Nobel Prize was awarded to Binnig and Rohrer in 1986 for building the first scanning tunneling microscope (STM) by utilizing tunneling current, the possibility of producing high-sensitive tunneling displacement transducers has been actively explored. Several years after the advent of the first tunneling transducer [8], sensors with a displacement resolution approaching $10^{-4} \text{ \AA} / \sqrt{\text{Hz}}$ were developed by Waltman [9] and Kenny [10]. In electron tunneling transducers, sub-angstrom changes in displacement induce measurable changes in tunneling current. This high sensitivity is independent of the lateral size of the electrodes because the tunneling current occurs between two metal atoms located at opposite electrode surfaces. Due to its high sensitivity and miniature size, a micromachined tunneling transducer makes it possible to fabricate sensors with high performance, small

size, light mass, and low cost. The sensors are in great demand in applications such as microgravity measurement, acoustic measurement, seismology, and navigation.

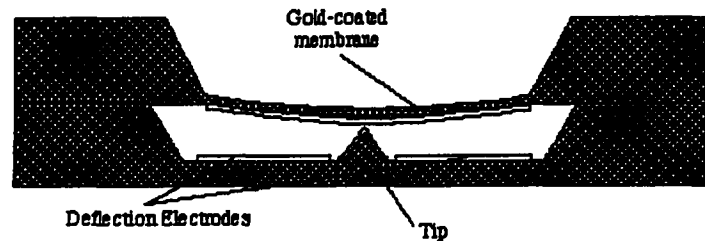


Figure 1-1 Cross-section schematic of a micromachined tunneling sensor

Since the advent of the scanning tunneling microscope (STM), much research [11][12][13] on transforming the high displacement sensitivity of the tunneling process into high sensitivity sensors have been made. Because tunneling only requires one metal atom on the surface of each side of the gap, this sensitivity is independent of the lateral dimensions of the electrodes. Therefore, many silicon micro-machined accelerometers with small size and light mass have been developed with high performance in both sensitivity and resolution [9][10][14]. Due to the strong distance dependence of the tunneling current, the tunneling effect is an attractive new technology for accelerometer instrumentation, which enables measurements of sub-Å scale displacements. Based on a STM design, the sensitivity of the tunneling current can be exploited to build relatively simple accelerometers. A typical membrane tunneling accelerometer is shown in Figure 1-1. The function is described following.

1.2 Objective

Because of the electron tunneling effect, the tunneling current could exponentially increase with displacement changes, by which tunneling sensors excel over most of the existing sensors, such as piezoelectric, capacitive, piezoresistive, and interferential

schemes. Also, the tunneling effect may happen between only two atoms, which make it possible to reduce the size and volume.

The use of PMMA as a kind of elastomer has drawn a lot of attention for softlithography and micro- to nano-fabrications. The reasons are clear: The price of PMMA is less than \$0.1 per square inch, which is ten times less than that of the Silicon. The bond temperature is about 150 °C, much lower than that of silicon bond temperature. It is easier to seal between PMMA-to-Si surface than between Si-to-Si surface. The PMMA is softer than Silicon and therefore more easily machined. The compatibility to bioorganic material and applications makes the PMMA welcome over Silicon. And the low cost in entry research encourages PMMA-related innovations.

The hot embossing technique intended for quick fabrication and high product rate is also employed. Due to the repeated use of templates in hot embossing, the cost of mold fabrication can be neglected in the whole process. The unlimited replication of structures from template to PMMA makes it a real mass-production process. In addition, the whole time for such a replication is less than 30 minutes, which is rather quick compared to silicon processing.

All in all, the objective of this project is to argue for the use of polymer, instead of silicon, to fabricate an inexpensive, batch-fabricated, high-yield and high sensitive tunneling displacement sensor. The first step of this project is to get 1-D vertical devices (sensitive to Z axis normal to wafer surface). Lateral 1-D and 2-D devices will be fabricated elsewhere in same research group. The ultimate goal of this project is to acquire 3-D micro sensor platforms for different kinds of applications. Once the polymer

sensor platform is implemented, five application areas will be considered to take advantage of the potential of this advanced MEMS technology. They are the accelerometer, the chemical sensor, the IR (infrared Radiation) sensor, the displacement sensor, and the magnetic sensor. The Accelerometer will be the first structure under consideration because of its simplicity.

1.3 Methodology

The metal tip and the counter electrode construct a tunneling junction. Under low-bias regime (millivolt) and vacuum conditions, the tunneling current, I , varies exponentially with the gap size S [Å]. The formula is written as:

$$I \propto V \exp(-\alpha s \sqrt{\Phi})$$

Where, Φ [eV] is the height of the tunneling barrier (or work function), V is the bias voltage, and α is $1.025[\text{Å}^{-1} \text{ eV}^{-1/2}]$. Let us give an estimation about the current changes corresponding to the gap changes. For the Au electrode, we have work functions of 5.1 eV (110) and 5.31 eV (111). If we take Φ as 5.2 eV, we have $e^{-2.337}=10.35$ when there is 1 Å gap change. That is to say that the current decays about one order of magnitude for each Å change. Therefore, if there is one-tenth change in current, we can measure a 10^{-2} Å gap change in distance. By the aid of mass proof, we can easily find a μg resolution for an accelerometer. If we keep constant tunneling current, we can easily

get: $const = \frac{d \ln V}{ds}$

This means we can get the exponential relationship between the bias voltage and the separation gap. The formula above is useful when proving the tunneling effect and feed back control in a closed loop measurement.

1.4 Process Instruments and Measurement System

1.4.1 Photolithography and Clean Room

Positive photo resist PR 1813, one of the S1800 Series Photo Resists, is mostly used in our clean room. Microposit S1800 Series Photo Resists are positive photoresist systems engineered to satisfy the microelectronics industry's requirements for the fabrication of advanced IC devices. The system has been engineered using a toxicologically safer alternative casting solvent to the ethylene glycol derived ether acetates. The dyed photoresist versions are recommended to minimize notching and maintain line width control when processing on highly reflective substrates.

The features of Microposit S1800 Series photo resists are similar and listed as follows:

Product Assurance

- Lot-to-lot consistency through state-of-the-art physical, chemical, and functional testing

- Filtered to 0.2 um absolute

Coating properties

- Cellosolve acetate and xylene free
- Striation-free coating
- Excellent adhesion

- Excellent coating uniformity
- A variety of standard viscosities are available for single-layer processing

Exposure properties

- Optimized for G-line exposure
- Effective for broad-band exposure
- Reflective notch and linewidth control using dyed versions

Development properties

- Optimized for use with the Microposit MF-319 metal-ion-free developer family
- Compatible with metal-ion-bearing microposit developers
- Removal property
- Residue-free photoresist removal using standard microposit removers

The optimized condition for photolithography is listed in Table 1-1.

Table 1-1. Optimized Conditions for PR1813

High resolution process parameters	
Substrates:	Silicon
Photoresist:	Microposit S1813 Photoresist
Coat:	1.23 μm
Softbake:	115 °C/60 sec, hotplate
Exposure:	G-line (0.54 NA), 150 mJ/cm ²
Development:	MF-319 15+50 sec. @21 °C

Negative photoresist NR9-1500P is also used when necessary. The negative photoresist process is described here:

It is essential to have a clean and dry wafer surface for a good photoresist adhesion. Initial cleaning and baking at about 200 °C for 15 to 20 minutes on a hot plate

is required immediately prior to the photoresist application (except in cases when wafers were taken directly from oxidation furnace or E - beam evaporator).

An additional surface treatment with hexamethyldisilazane (HMDS) adhesion promoter may be necessary in some cases:

- Place wafers in a desiccator containing a small beaker with HMDS.
- Connect desiccators to vacuum line.
- Keep wafers in desiccators under vacuum for ~ 5 minutes.

Photoresist application

- Negative photoresist: Futurrex NR9 – 1500P.
- Fill pipette with resist to about 1.5 inch and dispense on wafer.
- Spread, static, 2 seconds recommended; spin at 3000 rpm for 40 seconds (thickness ~ 1.0 μm).
- Soft bake at 130°C for 3 minutes on hot plate.
- Align mask and expose.
- Total energy required is ~ 200 mJ / cm². Measure intensity (mW/cm² at 366 nm wavelength) and calculate necessary exposure time: Intensity (mW/cm²) x Time (s) = Energy (mJ/cm²).
- Post bake at 100°C for 2 minutes on a hot plate.
- Develop by immersion and mild agitation in RD6 developer;
- developing time is ~ 8 seconds.
- Rinse in deionized (DI) water for 60 seconds immediately after developing. Spin dry. Inspect under microscope.

- If insufficiently developed, develop for 1 to 2 more seconds and check again.

Photoresist stripping: in oxygen plasma or with negative resist remover RR2.

The conditions for each way are shown in Table 1-2.

Table 1-2. Optimized Conditions for NR9 stripping

Oxygen plasma:	Negative resist remover:
Oxygen flow: 12 cc/min.	Heat solution to ~ 110 °C.
Power: 360 Watts	Place wafers in solution/5 min
Pressure: 380 mTorr	Rinse in DI water for 1 min
Time: 5 minutes	Spin dry and check

Clean room: A class-100 clean room is often used as work place for microfabrication. Here are some introductions to the clean room conditions and technologies:

Clean rooms are a work area with controlled temperature and humidity to protect sensitive equipment from contamination of air borne particles. Usually they are built with plastic walls and ceilings, external lighting, and a continuous intake of clean, particle free air. The room is cleaned daily to prevent further contamination.

Different industries require the use of a clean room. Medical facilities, integrated circuit manufacturers, and hard disk fabrication plants are just a few. Any firm which is involved with data recovery should have at least have a class 100 or better clean room to perform even the most basic recovery procedures.

Any class 100 clean room must adhere to strict control of the environmental conditions in order to insure a quality room. The environmental conditions in a clean room are controlled by positive air pressure, which is cleaned by a Hepa filter.

Equipment and diagnostic tools used in a clean room environment depend on the level of cleanliness needed. Many fabrication plants adhere to the established Federal Standard STD-209E. This standard outlines the airborne particulate cleanliness classes, so a class 100 clean room there would be no more than 100 particles (0.5 micron), in any given cubic foot of air.

The clean room is separated from the rest of the buildings air supply. It is ventilated with filtered air during construction to prevent contamination. Another risk factor is leakages in the system. To help guard against this, the Filter Fan Concept aids in the recalculation of about 96% of the total air volume within the clean shell and also ensures high flexibility.

Monitoring must be controlled 24 hours a day, and very closely during operation. Extremely sensitive measuring and testing equipment must be in place to ensure that the clean room is running properly, with no particulate above stated standard.

All operators are required to wear non lining body suits, shoes, gloves, head coverings and masks. Our clean room has a pass-through air blast/docking station, which because people represent the greatest influx of particle contamination and upon entering removes particles to ensure minimal contamination of the environment.

1.4.2 Hot Embossing

When manufacturing high-quality microstructures with a high aspect ratio from plastics by means of the LIGA method (LIGA is a German acronym for X-ray lithography, electrodeposition, and molding. In this technique, X-rays are used to carve

out deep patterns in a resist), there are three means for molding: reacting injection molding, injection molding, and hot embossing molding.

Hot embossing is the process of pressing a mold into a pre-fabricated semi-finished plastic product that is located on a substrate under vacuum. The process takes place at a temperature that ensures sufficient fluidity of the plastic materials. After the mold insert, the plastic material is cooled down to a temperature, which provides for a sufficient strength so the microstructured plastic material can be demolded. Figure 1-2 depicts the process steps of hot embossing.

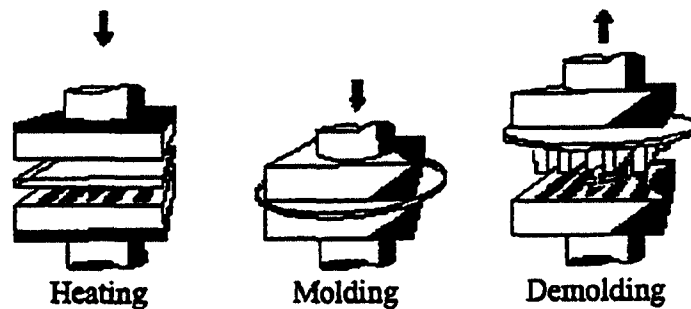


Figure 1-2 Process of hot embossing

Compared with injection molding, hot embossing has several significant advantages:

- The small deformation rates arising during molding result in small low velocities, which facilitate the molding of very fine structures without deformation occurring.
- Because the process conduct is close to the thermal equilibrium and the order of structural height has small flow path, the internal stresses in the molded plastic material can be minimized.

- Precise control of the process parameters, such as molding forces and temperatures, allows manufacturing microstructures with very thin, unstructured carrier layers.

Because a flowable state in enhancing temperature is needed, only thermoplastic amorphous (ex. PMMA) or semi-crystalline plastics (ex. POM) are suited for embossing. For amorphous plastics there exist glass transition temperature, T_g , and crystalline melting temperature, T_m . Semi-crystalline plastics show only a sharp decrease of strength in melting temperature (Shown in Figure 1-3). When filling the micro cavities in the embossing process and setting a certain carrier layer thickness, certain fluidity must be reached. In the case of semi-crystalline plastic material, the fluidity may be achieved in a narrow temperature range above the crystallite melting temperature. When amorphous polymers are concerned, the embossing temperature is mostly far above the glass temperature.

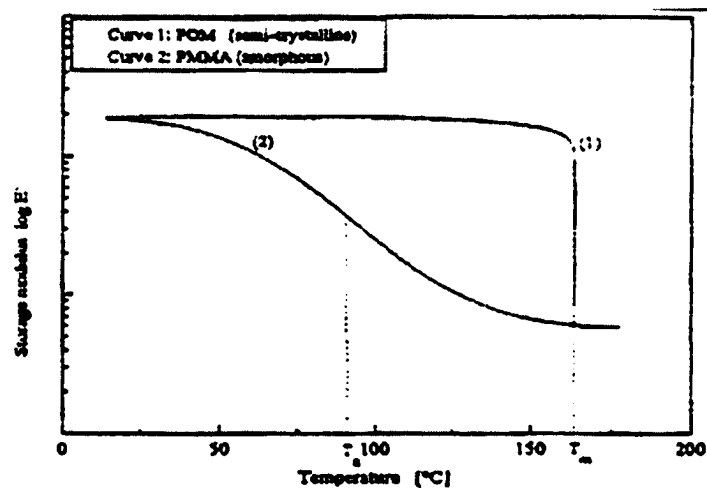


Figure 1-3 Thermo-mechanical behavior of material

By reducing the process temperature to below the glass temperature in the case of amorphous plastics and below the melting temperature for semi-crystalline plastics, an increase in the mechanical strength of the plastic material is achieved. In the case of amorphous plastics, a demolding temperature far below T_g must be reached due to the larger softening range, which means smaller cycle times can be attained for semi-crystalline plastics compared to amorphous plastics.

During demolding, if the demolding stress exceeds the yield stress of the plastic materials, tear off and shearing as well as distortions and deformations may occur in the demolding direction of the microstructures. The generation mechanisms of demolding stress are of variable nature. Mostly, they are heat-induced stress, tension or compression induced stress, and mold deformation induced stress.

Here is a primary means to minimize the demolding stresses. Taking into account the temperature influence on the material data, the developing demolding stresses can be described as follows [15]:

$$\sigma = \sigma_D + \int_{T_d}^{T_g} \frac{E_p(T)}{1 - 2\nu_p(T)} (\alpha_{th,p}(T) - \alpha_{th,M}(T)) dT \quad \text{where,}$$

σ : demolding stress; E_p : Young's modulus; ν_p : Poisson's ratio (plastic) $\alpha_{th,p}$: thermal expansion coefficient (plastic); $\alpha_{th,M}$: Thermal expansion coefficient (mold); T_d, T_g : demolding and glass temperature.

The mathematical solution for the above equation is complicated. We can follow the experimental steps:

- First we get the p (pressure), v (volume), T (temperature) diagram of the plastics as a function of temperature. The thermal expansion coefficient can be obtained from the slope of the curve.
- To minimize the demolding stresses that may cause structure distortions, the demolding temperature must be avoided where abrupt changes of expansion occur.
- We also need to plot Young's modulus dependence of temperature, where we should choose a proper temperature to keep a sufficiently high mechanical strength for applying demolding forces to the plastic material.
- By use of the equation above as well as these two plots, we plot demolding stresses as a function of temperature and Young's modulus. With the purpose of reduction of demolding stresses, we can determine the appropriate demolding temperature for optimum molding of microstructures.

More discussion about PMMA (Poly methyl methacrylate) and POM (Poly Oxy methylene) can be found in reference [16].

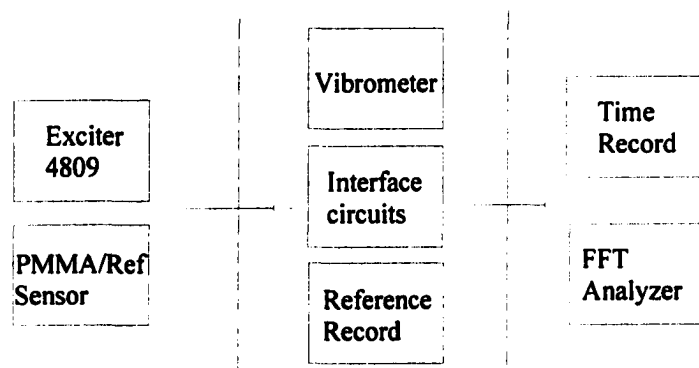


Figure 1-4 Function illustration of measurement

1.4.3 Measurement System

The function blocks of the measurement system is plotted in Fig. 1-4, which includes three function blocks of generation, calibration, and analysis. The exciter 4809 produces acceleration by aid of a service instrument, which is installed on an anti-vibration station. The fabricated tunneling sensors together with a reference accelerometer record the original signal and generate time, frequency, and noise information. The laser vibrometer gives out the exact displacement of proof mass, which is used for identification of the tunneling work function. The control and feedback circuit shows the measured value and helps to control the sensor at a stable condition. The oscilloscope and vib-analyzer measure the output signal and analyze the sensor information.

Operation Principle of VDD 650 Vibrometer. Polytec's Vibrometer with Digital Demodulation (VDD) is a PC-based signal processing system, which adds the option of digital demodulation of the Doppler signal from the optical sensor to Polytec's laser vibrometer. The digital signal processing technology of the VDD 650 enables you to decode the measured quantities of displacement, velocity, and acceleration with a degree of precision and a resolution that a conventional laser vibrometer would not be capable of. Through immediate integration of signal decoding and signal evaluation in the PC, the system VDD 650 works without additional signal conversion and signal transmission, both of which can have a negative effect on the high level of accuracy attained when measuring with the laser Doppler method.

Signal decoding in the VDD 650 is carried out using purely numerical methods in the PC. This signal processing method requires the Doppler signal being made available as a two-channel quadrature signal, also known as an I&Q signal. This type of signal is familiar from classical interferometers used for length measurement, and from other incremental sensors. As, however, the heterodyne interferometer used in the optical sensor generates the Doppler signal as a one-channel carrier frequency signal, this initially has to be converted electronically into an equivalent I&Q signal. The signal conversion is done in the digital front end. The I&Q signal pair is run from the interface EXTENSION on the back of the digital front end via the junction box VDD-Z—1- to two synchronously sampled input channels on the data acquisition board in the PC. Here, the I&Q signal pair is translated into two data streams with an amplitude resolution of 12 bit and a maximum sampling rate of 5.12 Msa/s. If required, the reference signal is acquired by another input channel, the resolution of which is between 12 bit and 16 bit, depending on the selected analysis bandwidth.

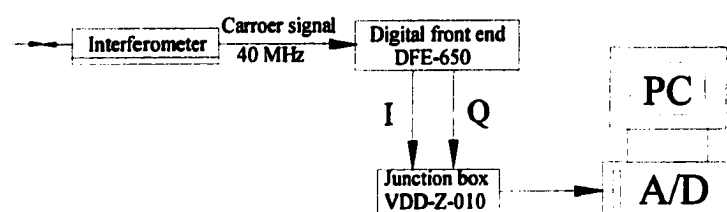


Figure 1-5 Scheme of the PC-based digital vibrometer system VDD 650

The metrological properties attained by the VDD system are primarily determined by the algorithms for the numerical decoding of the Doppler information implemented in the software VibSoft. In this connection, the amplitude resolution and accuracy of the

A/S converter only have a negligible influence on the properties of the system, in contrast to the conventional acquisition of the analog measurement signals. The nominal resolution of the data acquisition board of 12 bit is thus not directly connected to the resolution and the measurement range of the whole system which can be attained. Residual errors from the A/D conversion are corrected in the VDD while decoding with the aid of the mathematical methods.

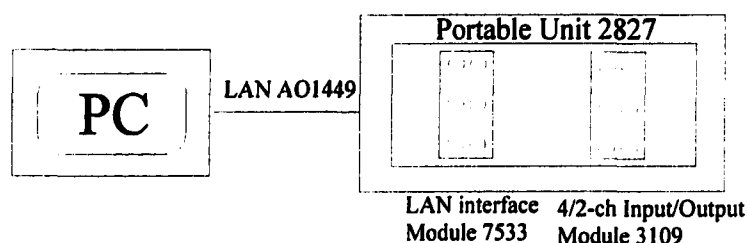


Figure 1-6 Portable PULSE measurement system

After decoding, which primarily provides the displacement signal, a reduction of data is carried out initially, which adapts the output data rate to the analysis bandwidth required. With VibSoft set appropriately, the displacement signal is also used to calculate the velocity or acceleration information in the time domain with a high degree of accuracy through single or double differentiation. With the aid of digital filter functions, noise components can be removed from the time signal. At the same time, a high-performance two channel FFT analyzer is available for signal analysis in the frequency range. The measurement data from the VDD is not available online but can be exported in various formats. The diagram of VDD 650 function is plotted in figure 1-5.

The Multi-analyzer system type 3560C—PULSE is the product of Brül & Kjær Company for PULSE analysis. The system (type 3560C) consists of a PC with LAN

interface, Pulse software, Windows NT/2000, Microsoft Office, and IDA Data Acquisition Front-ends hardware. The system can contain up to 128 input channels located in up to ten front-ends of the same or different type. (See figure 1-6) Our system specifically contains:

- PULSE DATA ACQUISITION SYSTEM for 2 input channels for FFT analysis, and 1 output signal generator (sine, sine sweep, random, pseudo-random), auto and Cross-Spectrum calculations, with 1 reference signal, and 25.6 kHz frequency range.
- Type 2827 Portable Acquisition Frame for 3560C. Can be operated with two QB0048 batteries (not Included).
- Type QB0048 Batteries. Rechargeable Ni-MH Batteries for 2827. The 2827 can hold two QB0048 batteries.
- Type 7533 10Mbit LAN Interface Module, 150 kHz bandwidth, 1ch Input.
- Type 3109 4/2-Channel Input/Output Module. Four channels with BNC/LEMO connections for direct, DeltaTron/IsoTron, and microphone inputs. Two channels for generator outputs.
- Type 7770G Noise and Vibration Analysis Software, 2 Channel License, FFT Analyzer.
- Type UL0166NA2 Dell Computer C610 Minimum specs 1GHz PIII, 256MB RAM, 20GB HD, CD-ROM, Ethernet/modem, Windows 2000 Pro, MS Office XP Pro (max 75 beats). The analyzer is a PC based analyzer. The hardware

includes the acquisition front-end, and the software on the PC controls the hardware and the channels.

Also, a shaker system to produce exciter signal and accelerometer is included:

- Type 4809 Vibration Exciter system, 45N Force Rating, Frequency range 10Hz to 20 kHz. Very Low rocking motion and transverse vibration of the moving part.
- Type 2718 Power Amplifier system for the drive of shaker 4809, Low distortion, and flat frequency response from 10Hz to 20 kHz (+-0.5dB). Signal generated by the PULSE analysis system and connected to the Power Amplifier.

CHAPTER 2

STRUCTURE DESIGN AND SIMULATION

2.1 Design Methodology

The design flow chart for the accelerometer is shown in Figure 2-1. The chosen method of tunneling effect can indicate a Z-axis sensitivity of the device. This Z-axis sensitivity then indicates the size and the geometry of the proof mass, tip, and other process condition. The open loop character is then inspected. The tunneling current-gap relation should be obtained. Then, with proper design of feedback circuits, together with parameter changes and electrostatic actuator utility, a closed loop system is obtained. And accelerometer is marked with the help of gravimeter.

2.2 Design of Manufacturing

Figure 2-2 is the cross-section sketch of tunneling accelerometer. The sensor itself is made up of PMMA. The proof mass has a specific size and mass. Because Au has a stable identity, we use Au film as the electrode. A layer of Ti (about 0.3 nm) is sputtered for better adhesion between Au metal electrode and PMMA. The tip and the counter electrode compose the tunneling structure. The deflection electrode and the counter electrode adjust the distance of the gap. The adjusting force is electrostatic force. When operating, the device works by applying an offset voltage to the deflection electrode to electrostatically deflect the proof mass fixed on the membrane towards the tip. When a

small tunneling current appears between the tip and the counter electrode, the device is operated at open loop condition. The relation between tunneling current LnI (or LnV) and distance of the gap is checked to prove the tunneling effect. Then a feedback voltage is added to the offset voltage on the deflection electrode to maintain the current at a constant value. When an external force is applied to the proof mass, the feedback circuit responds by applying a balancing electrostatic force. The external forces are determined by monitoring the feedback control voltage.

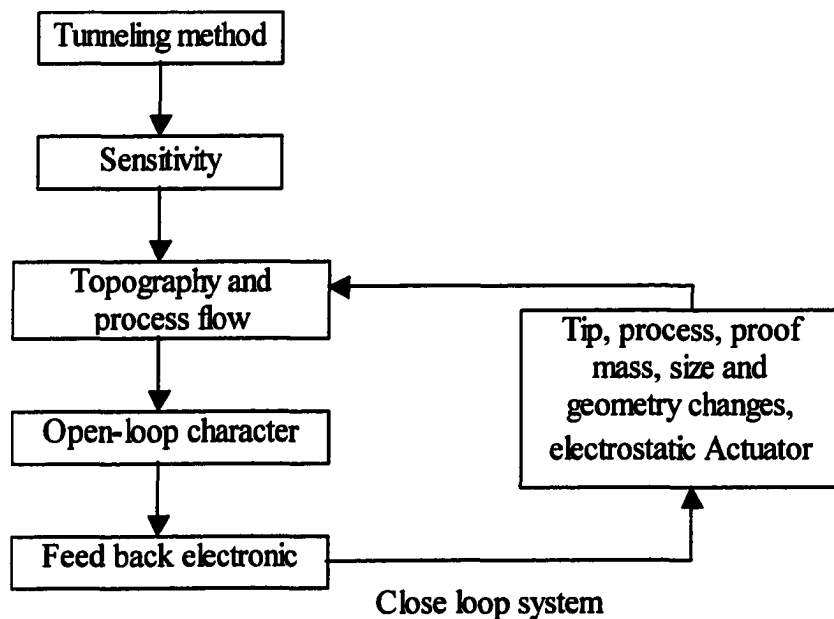


Figure 2-1 Design flowchart

The complete fabrication process has been presented in figure 2-3. Figure (a) and (b) are for top parts. The structure is obtained directly by hot embossing with proper sizes of proof mass and lateral lengths. The thin sheet is then grounded into thinner membrane by mechanical and RIE etching. The Ti/Au layer is sputtered thereby. For the lower part, which is shown in figure (b) and (c), the processing is more simple. Just get the structure

directly from hot embossing and then pattern the electrodes after metal film deposition. Finally, these two parts are bonded together by epoxy glue. Detailed descriptions can be found in chapter four.

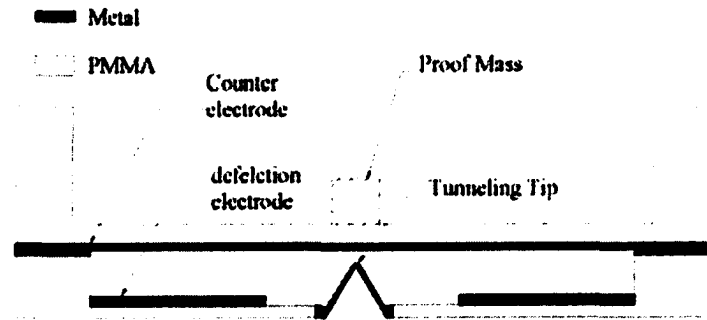


Figure 2-2 Cross section of vertical tunneling accelerometer

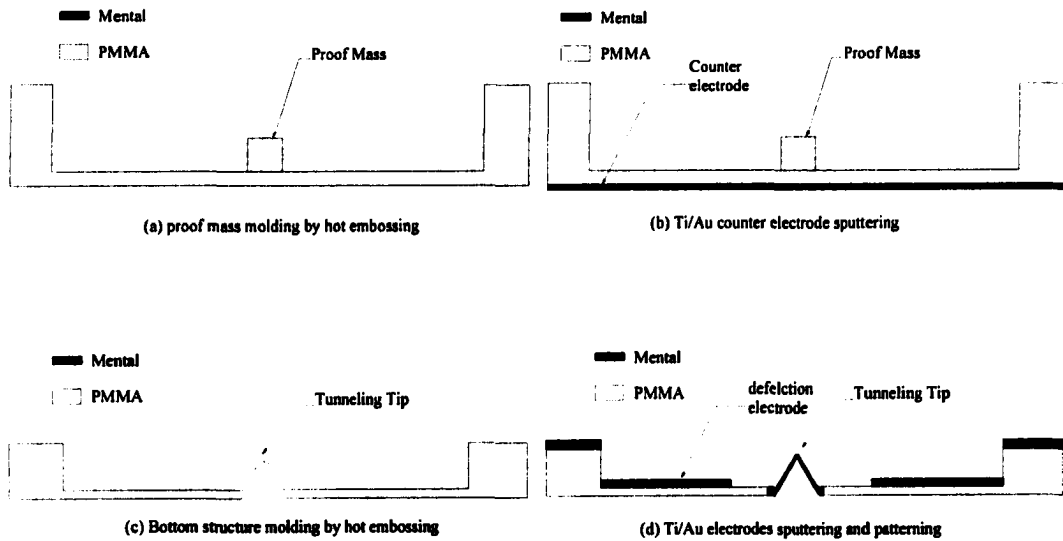


Figure 2-3 Processing flow chart for PMMA tunneling sensor

2.3 tProof mass and Mechanical Simulation by ANSYS

2.3.1 Introduction to ANSYS

The ANSYS Product Suite includes its time-tested, industry-leading applications for structural, thermal, mechanical, computational fluid dynamics, and electromagnetic analyses, as well as solutions for transient impact analysis. ANSYS software solves for the combined effects of multiple forces, accurately modeling combined behaviors resulting from "Multiphysics" interactions. The software also features advanced nonlinear material simulation and the best solvers money can buy.

MEMS is an abbreviation for Micro Electro Mechanical Systems. MEMS technology is at the center of a rapidly emerging industry combining many different engineering disciplines & physics: electrical, electronic, mechanical, optical, material, chemical, and fluidic engineering disciplines. As the smallest commercially produced "machines", MEMS devices are similar to traditional sensors and actuators although much, much smaller. The broad physics capability of ANSYS/Multiphysics has been progressively enhanced to meet the unique simulation requirements of the Microsystems / MEMS device designer.

As parts of multiphysics subfunctions, Mechanical and Structural analysis are necessary in my research. Thanks to its full complement of nonlinear elements, nonlinear and linear material laws, and inelastic material models, ANSYS/Structural easily simulates even the largest and most intricate of structures. Plus, its world-class nonlinear contact functionality allows for the analysis of complicated assemblies. ANSYS/Structural offers users an intuitive, tree-structured GUI for easy definition of

even the most intricate material models and a choice of iterative and direct solvers for optimal results (Note: Supplementary solvers may be added via the Parallel Performance for ANSYS module.) On the other hand, ANSYS/Mechanical includes a full complement of non-linear and linear elements, material laws ranging from metal to rubber, and the most comprehensive set of solvers available. It can handle even the most complex assemblies—especially those involving non-linear contact—and is the ideal choice for determining stresses, temperatures, displacements and contact pressure distributions on all your component and assembly designs.

2.3.2 Static Analysis

Static analysis is used to determine the displacements, stresses, strains, and forces in structures or components caused by loads that do not induce significant inertia and damping effects. *Steady* loading and response conditions are assumed; that is, the loads and the structure's response are assumed to vary slowly with respect to time. The static analysis describes the changes when a force or other kinds of loadings are applied onto the structures. The structures are treated as ideal elements by “meshing” nodes without inertia and damping. Also, the time varying load is analyzed later.

As shown in figure 2-4, the key parts of movement are thin sheets of proof mass located at the center. The four areas of sheet edges have zero displacement because of the connection with substrate bulk. The applied force or acceleration is applied onto the whole area with a vertical direction of Z. When the sheet thickness is about 20 to 50 μm , and the height of proof mass is about 50 to 60 μm , all the items are seen as “block” instead of “sheet”, which, however, greatly slows down the speed of analysis simulation.

Because the force is a kind of field existing everywhere of the sensor, the force is loaded as a static force instead of a point force. The maximum displacement at Z direction can be obtained from the analysis and is used for the calculation of spring constant K .

Table 2-1. Structure Parameter with Simulated K Values

Sheet parameter	X (m)	Y (m)	Z (m)	K (N/m)
M=2.3E-7 kg F=1E-6N D=1150 (kg/m ³) Sheet size: 2mm,2mm,50um	0.00E+00	0.00E+00	0.00E+00	12.77043
	2.00E-04	2.00E-04	5.00E-05	5.810744
	4.00E-04	4.00E-04	5.00E-05	6.778926
	6.00E-04	6.00E-04	5.00E-05	9.226624
	8.00E-04	8.00E-04	5.00E-05	11.65925
	1.00E-03	1.00E-03	5.00E-05	17.01505
M=9.2E-8kg F=1E-6N D=1150 (kg/m ³) Sheet size: 2mm,2mm,20um	0.00E+00	0.00E+00	0.00E+00	12.77043
	2.00E-04	2.00E-04	5.00E-05	0.118318
	4.00E-04	4.00E-04	5.00E-05	0.159804
	6.00E-04	6.00E-04	5.00E-05	0.222509
	8.00E-04	8.00E-04	5.00E-05	0.334351
	1.00E-03	1.00E-03	5.00E-05	0.491777
M=2.07E-7 kg F=1E-6N D=1150 (kg/m ³) Sheet size: 3mm,3mm,20um	0.00E+00	0.00E+00	0.00E+00	0.024473
	2.00E-04	2.00E-04	5.00E-05	0.029583
	4.00E-04	4.00E-04	5.00E-05	0.592624
	6.00E-04	6.00E-04	5.00E-05	0.765562
	8.00E-04	8.00E-04	5.00E-05	0.658605
	1.00E-03	1.00E-03	5.00E-05	0.863126
M=3.68E-7 kg F=1E-6N D=1150 (kg/m ³) Sheet size: 4mm,4mm,20um	0.00E+00	0.00E+00	0.00E+00	0.027666
	2.00E-04	2.00E-04	5.00E-05	0.100214
	4.00E-04	4.00E-04	5.00E-05	0.158581
	6.00E-04	6.00E-04	5.00E-05	0.10161
	8.00E-04	8.00E-04	5.00E-05	0.1777
	1.00E-03	1.00E-03	5.00E-05	0.205081
M=8.28E-7 kg F=1E-6N D=1150 (kg/m ³) Sheet size: 6mm,6mm,20um	0.00E+00	0.00E+00	0.00E+00	0.011623
	2.00E-04	2.00E-04	5.00E-05	0.028607
	4.00E-04	4.00E-04	5.00E-05	0.026068
	6.00E-04	6.00E-04	5.00E-05	0.017345
	8.00E-04	8.00E-04	5.00E-05	0.027685
	1.00E-03	1.00E-03	5.00E-05	0.02722

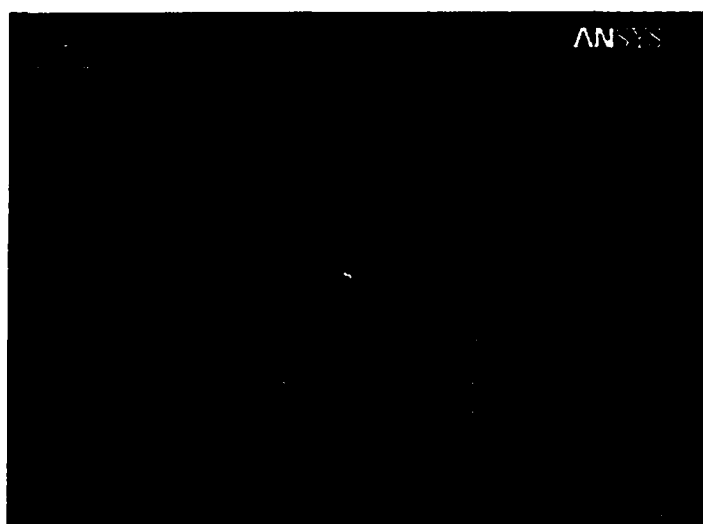


Figure 2-4 Structure schematic and loading conditions at static analysis

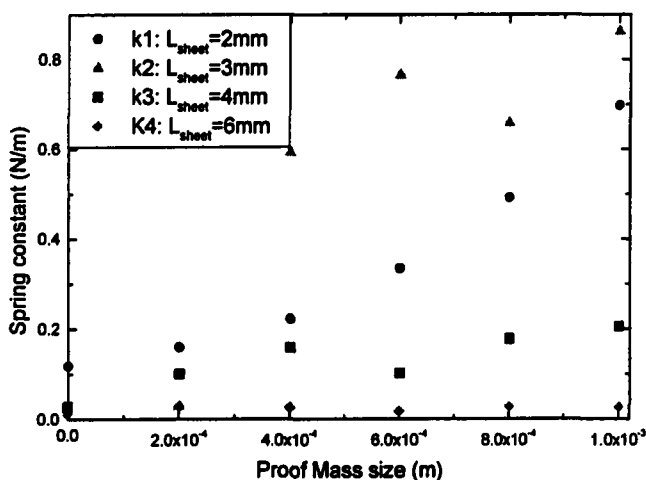


Figure 2-5 Spring constant versus proof mass size at different sheet parameters

Several sizes, thicknesses, and heights of sheet and proof mass were chosen and are listed on table 2-1. The corresponding plots of spring constant k v.s. sheet length are showed in figure 2-5. From the plot of figure 2-5, the spring constant k changes a lot when either the sheet parameters or the proof mass changes. However, the main condition

to determine the k values is the sheet parameters in magnitude scale while the proof mass only changes one to two times. The scale rule of structure with features is important when optimizing the characteristics of transducer. A detailed discussion can be found later.

2.3.3 Model Analysis

We use model analysis to determine the vibration characteristics (natural frequencies and mode shapes) of a structure or a machine component while it is being designed. It can also be a starting point for another, more detailed, dynamic analysis, such as a transient dynamic analysis, a harmonic response analysis, or a spectrum analysis.

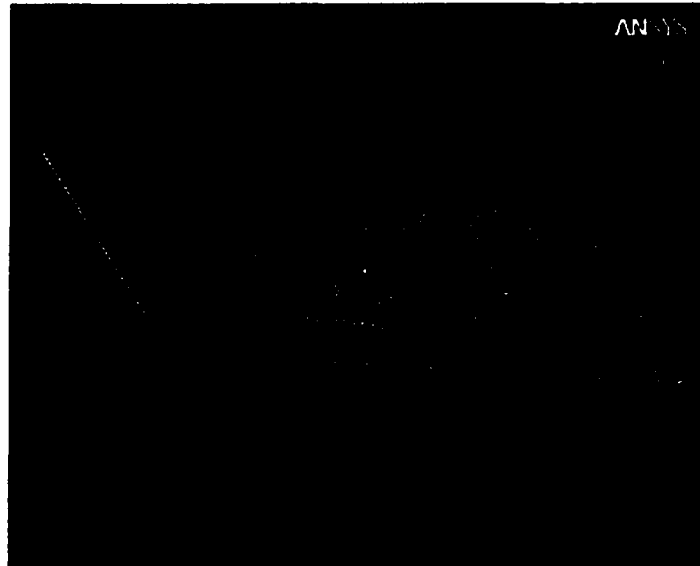


Figure 2-6 First vibration model simulated by AnSys

The natural response of the mechanic system is so important that it gives out almost all the dynamic properties of the structure. The frequency upper limit is determined by the system natural frequency and other characteristics, such as spectrum analysis, mode harmonic and transient response, are all related. The model analysis provided by ANSYS is a linear analysis, which helps to determine the vibration

characteristics of the structure. The damping or pre-stressed structures can also be included when model analysis is performed.



Figure 2-7 Second vibration model simulated by AnSys

The structure is constructed as $4\text{ mm} \times 4\text{ mm} \times 20\text{ }\mu\text{m}$ sheets together with a $400\text{ }\mu\text{m} \times 400\text{ }\mu\text{m} \times 50\text{ }\mu\text{m}$ proof mass. The applied force is added by a way of pressure because the force field is applied on total upper area instead of one point or all-nodes. A good way to estimate acceleration to pressure is as follows:

$$P = \frac{a \cdot d \cdot V}{S}; \text{ Where, } a \text{ is applied acceleration, } d \text{ is material density, } V \text{ is material}$$

volume and S is sheet area. Then one mili-g acceleration is about 2.3×10^{-3} Pa.

Four possible vibration models are simulated. The first model is natural response to applied force, which is about 150 Hz (Shown in figure 2-6). The resonant frequency is important in that it reflects both the open loop spring constant and the maximum sensitivity. More discussion about natural frequency is found in Chapter 3.

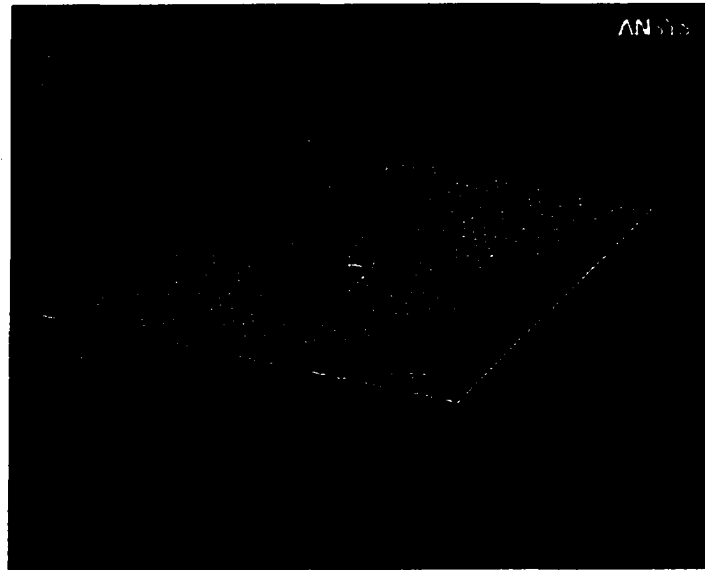


Figure 2-8 Twist as third vibration model by AnSys



Figure 2-9 Fluctuation as the fourth vibration model by AnSys

The second vibration model is shown in figure 2-7. The torque produced by corner makes the twist toward two corners. The corresponding frequency is about 1680 Hz, which is higher than natural frequency. In order to avoid the twist, the sampling frequency should be lower than the first resonant frequency.

A third vibration model is plotted in figure 2-8. This twist is produced by edge torque, which excites a frequency of 17315 Hz. This is such a high model that there is no response at all expected disturbance.

The last vibration model is a wave-like fluctuation (shown in figure 2-9). The four corners fluctuate up and down in pairs. The corresponding frequency is about 26135 Hz, which is also high enough to be omitted because of a low exciter frequency of less than 150 Hz.

2.3.4 Harmonic Response

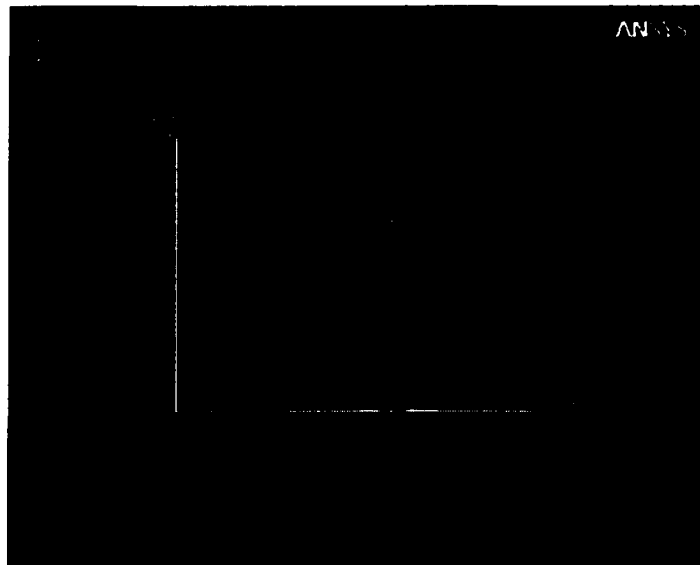


Figure 2-10 Displacement response vs. frequency

Harmonic response analysis is a technique used to determine the steady-state response of a linear structure to loads that vary harmonically with time. The idea is to calculate the structure's response at several frequencies and obtain a graph of some response quantity (usually displacements) versus frequency. "Peak" responses are then identified on the graph and stresses reviewed at those peak frequencies. Three harmonic

response analysis methods are available: *full*, *reduced*, and *mode superposition*. The *full method* is the easiest of the three methods. It uses the *full* system matrices to calculate the harmonic response (no matrix reduction). The matrices may be symmetric or asymmetric.

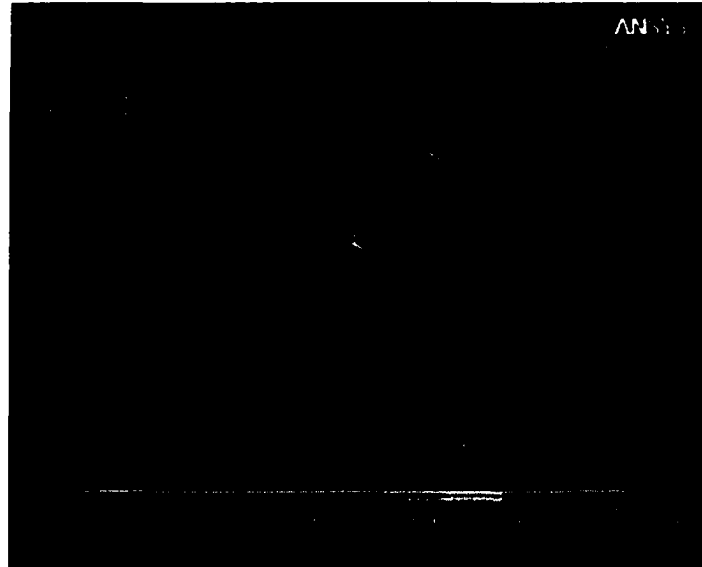


Figure 2-11 Displacement contour plot at 1 *mg* acceleration

Fifty frequencies near natural frequency are calculated and the center point displacement changes are given out in figure 2-10. When the excited frequency is lower than 100 Hz, the maximum displacement is about 10^{-5} meter (Applied force is 1 Newton, rather large compare to the real value). When the frequency is near the resonant value of 150 Hz, the displacement response rises greatly and reaches its maximum value of two degrees larger in magnitude. This maximum value is also distributed differently over the entire sheet. A contour plot (figure 2-11) of displacement can tell that the center point is the greatest in magnitude. The plot also shows that the distribution is center symmetric.

2.3.5 Static Force and Bending

Table 2-2. Electrostatic Deflection Summary

Area (um ²)	Gap (um)	PMMA (um)	Voltage (V)	Gold (um)	Displacement (um)
500*500	50	20	100	2	0.322757
500*500	50	20	200	2	1.38
500*500	10	20	100	2	139.947
500*500	10	20	50	2	3.901
500*500	15	20	100	2	20.993
500*500	15	20	50	2	0.993301
500*500	15	50	100	2	0.323847
500*500	15	50	200	2	1.532
2000*2000	15	50	100	2	1.43
2000*2000	15	50	150	2	5.472
2000*2000	20	50	100	2	1.386
2000*2000	20	50	150	2	3.897
2000*2000	15	70	100	2	0.537061
2000*2000	15	70	150	2	1.316
2000*2000	15	70	200	2	2.788
2000*2000	15	100	200	2	0.877284
2000*2000	15	100	250	2	1.463
2000*2000	15	100	300	2	2.333
2000*2000	50	50	200	2	0.446758
2000*2000	50	50	300	2	1.024

The relation between stress distribution and applied force induced by actuator voltage is so important that it constrains the spring limitation as well as the force tolerance. The maximum stress and strains distribution can be found in figure 2-12, which describes the stress as located mainly at center point. The maximum deform is about 2 μm when the actuator area is 0.5 mm \times 0.5 mm with a distance of 15 μm . The applied voltage is about 50 V, which produces an actuation ratio of 0.04 μm per volt. Moreover, for a parallel plate capacitor, the electrostatic forces are given by:

$F = \frac{\epsilon_0 A_a V_a^2}{2(g_0 + z)^2}$; where ϵ_0 is the electric permittivity, A_a is the actuator area; V_a is the applied voltage, and g_0 is the nominal gap. The calculation value from the parallel capacitor formula with the same sizes is 2.3 μm , which coincides well with the simulation value, though it neglects the dissipation of force because of edge effect.

The static force distribution is plotted in figure 2-13. The force is almost uniform at the center, and there is some dissipation at the edges. A simulated parameter list is plotted in Table 2-2, which gives a good estimation of electrostatic deflection summary.

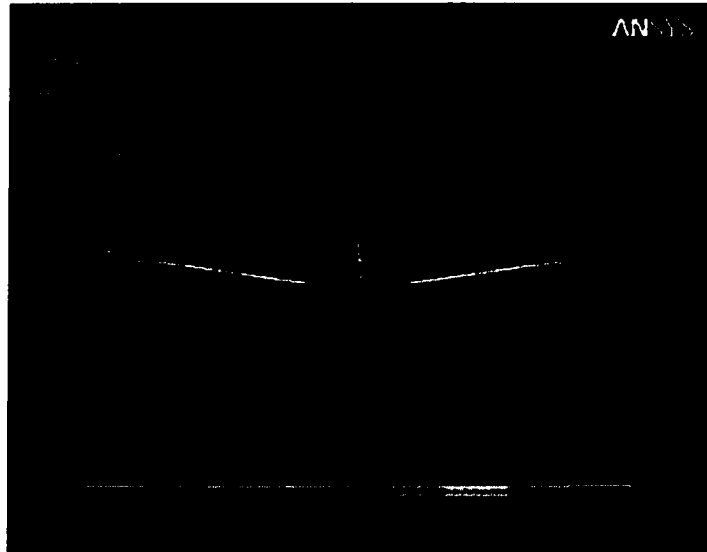


Figure 2-12 Deformation when 50 V applied on to actuator

2.3.6 Parameter Design Based on ANSYS

From the analysis by ANSYS, all the characteristics of a vertical tunneling PMMA accelerometer can be simulated before fabrication. The parameters of several sized sensors are listed in table 2-3. From the data, we can see the larger the sheet size, the lower the natural frequency. If we keep the sheet size constant, the natural frequency

is almost constant, while spring constants change about 10 times. A 4 mm×4 mm sheet with 200 μm square proof mass is the optimum condition.

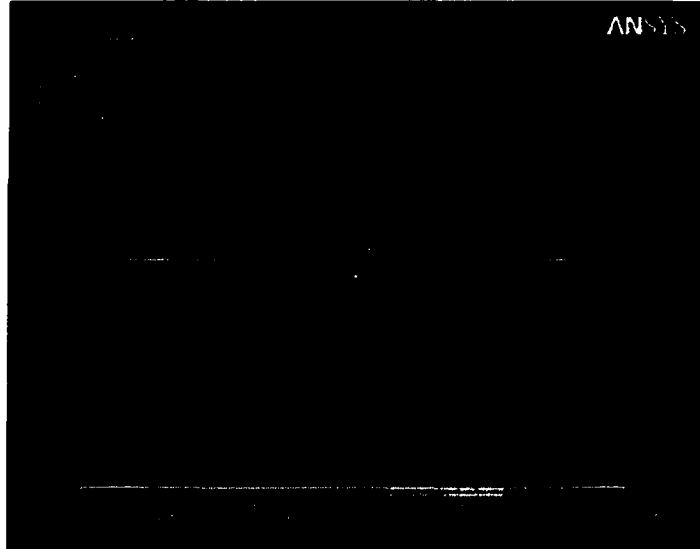


Figure 2-13 Static force distribution produced by actuator

2.4 Electronic Control and Feedback Circuit

The accelerometer operates at the constant current model. The tunneling current is sensed like a trans-impedance amplifier. The transfer function of this amplifier is given as

$$\frac{V_t}{I_t} = f(R, C, \omega),$$

where R, C is the sensor dynamic resistance and parasitic capacitance.

ω is the simulative frequency. The tunnel voltage then connects to a readout circuit and negative feed back actuation voltage is sent to the electrostatic actuation pad. When the sensor is accelerated, the proof mass experiences an inertial force, which causes its motion to lag that of the sensor. Generally, we operated with high gain to ensure the proof-mass motion was small (less than 1 Å) so the negative voltage of the amplifier could bring the tunneling tip closer to or farther from its counter-electrode. The feed back

circuit is simple, and many low pass amplifier circuits [17][18] can be followed. Figure 2-14 is one of them.

Table 2-3. Parameter List of Different proof Mass Sheet

Sheet size	Frequency (Hz)	Displacement	Spring constant
2mm sheet, 0 proof mass	4161	8.45E-06	0.118318
2mm sheet, 200 μ m P.M.	2148	6.26E-06	0.159804
2mm sheet, 400 μ m P.M.	2124	4.49E-06	0.222509
2mm sheet, 600 μ m P.M.	2168	2.99E-06	0.334351
2mm sheet, 800 μ m P.M.	2288	2.03E-06	0.491777
2mm sheet, 1000 μ m P.M.	2440	1.43E-06	0.697345
4mm sheet, 200 μ m P.M.	810.3	3.61E-05	0.027666
4mm sheet, 400 μ m P.M.	1204	9.98E-06	0.100214
4mm sheet, 600 μ m P.M.	1258	6.31E-06	0.158581
4mm sheet, 800 μ m P.M.	1054	9.84E-06	0.10161
4mm sheet, 1000 μ m P.M.	1164	5.63E-06	0.1777
6mm sheet, 200 μ m P.M.	434.7	8.60E-05	0.011623
6mm sheet, 400 μ m P.M.	620.3	3.50E-05	0.028607
6mm sheet, 600 μ m P.M.	539	3.84E-05	0.026068
6mm sheet, 800 μ m P.M.	468.9	5.77E-05	0.017345
6mm sheet, 1000 μ m P.M.	518.6	3.61E-05	0.027685

When the proof mass is within about 10 \AA of the tip, the tunnel current is about 1.5 nA from the tip to the counter electrode. So the pre-amplifier gain should be 6 to 7 orders in magnitude. Usually, the tunneling current is fed into a trans-resistance amplifier. This voltage signal is then compared to a reference signal proportional to the desired tunneling current. When there is a fluctuation in the gap, an error signal is produced which adjusts the actuator signal to control the tunnel gap. Therefore, the gap is controlled to a separation defined by the reference set point.

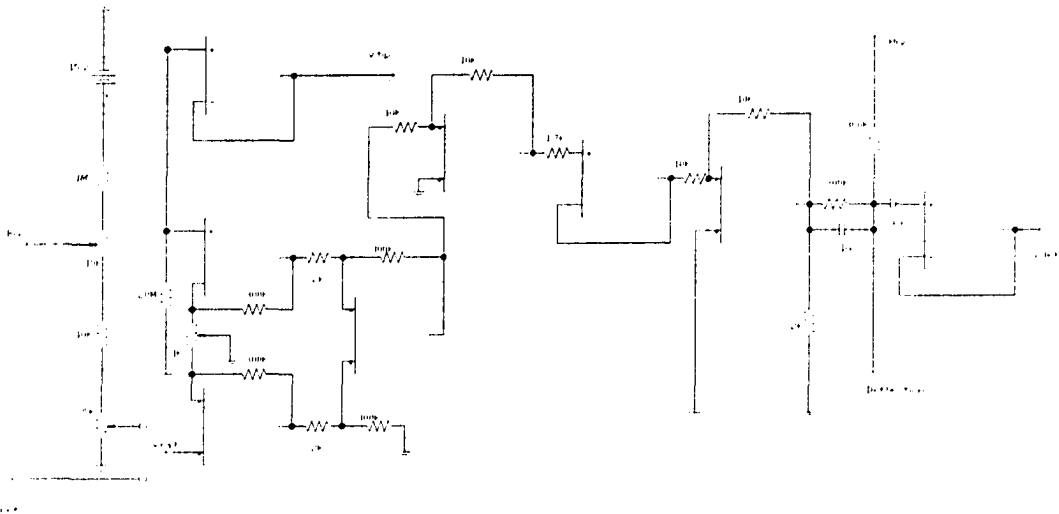


Figure 2-14 Feedback and control circuit for accelerometer

Two crucial problems need to be presented here. The first one is that feedback speed must be fast enough to respond, which requires an operation frequency lower than the natural oscillation frequency of the proof mass. In most cases, the natural frequency is described by: $\omega_n = 2\pi\sqrt{k/m}$. If we think all the deviation is small and the membrane vibrates at linear spring area, we can estimate the k/m ratio. Because we have $k\Delta z = m\Delta a$, k/m should be $\Delta a / \Delta z$. Following the estimated value Δa is about 10^{-6} g and

Δz is about 10^{-4} Å, we have ω_n to be about 10^4 r/s. So we can conclude that the proof mass automatically satisfies the response time requirement. Also, we can measure the natural frequency of system by operating it at open loop condition. So a low pass readout or preamplifier circuit is necessary.

The second problem is to consider the noise. From the study [19] of the noise spectrum, the dominant noise is low frequency noise, which is mainly generated by thermal expansion mismatch. So a relative higher operation frequency is reasonable. A 100~200 Hz operated frequency would be chosen.

CHAPTER 3

MODELING AND CONTROL SYSTEM

SYNTHESIS BY MATLAB

3.1 Introduction

Several years after the advent of the first tunneling transducer [8], sensors with displacement resolution approaching 10^{-4} Å/√Hz were developed by Waltman [20] and Kenny [9]. In electron tunneling transducers, a 1% change in 1.5 nA current between tunneling electrodes corresponds to a displacement fluctuation of less than 0.1 Å. This high sensitivity is independent of the lateral size of the electrodes because the tunneling current occurs between two metal atoms located at opposite electrode surfaces. Due to its high sensitivity and miniature size, micro machined tunneling transducers make it possible to fabricate a high performance, small size, light mass, inexpensive accelerometer, which is in great demand in applications such as microgravity measurements, acoustic measurements, seismology, and navigation.

Considerable research work on accelerometers [21] [22] [23] has been developed. However, most micro machined tunneling accelerometers still suffer the problem of enhancing resolution while broadening measurement bandwidth. Liu *et al* developed a controller design by μ -synthesis [24] which accomplished a high precision, wide-

bandwidth micro machined tunneling accelerometer [25]. However, the method is complicated and frustrating, especially to new device designers, who intend either to devise innovative tunneling sensors or to reconstruct revised structures for better performance. Because their purpose is not to accommodate different sensors for mass production like Liu's μ -synthesis method, a simple, effective and effortless design method is necessary. In this paper, a Computer Aided Engineering (CAE) tool, MatLab Simulink, is chosen as a kind of technical computing language to model and simulate the function of the tunneling accelerometer. After approximation at small signal input, a simpler means to synthesis control systems is established. The designed transfer function is evaluated and compared with the real system. At the same time, some simulation results of the mechanical performance, frequency response, system stability, time history, and dynamic range of tunneling accelerometers are plotted and discussed. Moreover, since the design and analysis of control systems could be done prior to the micro machining process, further research and mass production processes can be greatly expedited and streamlined.

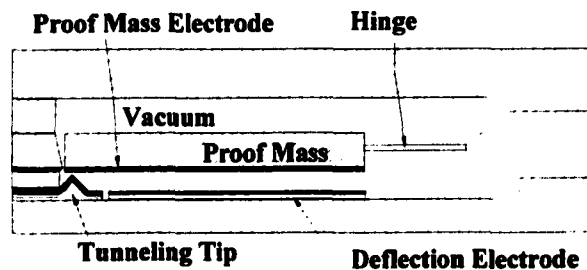


Figure 3-1 Cross section schematic of micromachined tunneling accelerometer

3.2 Accelerometer Structure

A typical tunneling accelerometer has mechanical components and three electrodes. In order to simplify the situation, the silicon based cantilever type accelerometer is analyzed here. The mechanical components comprise a fixed cantilever with a tunneling tip on the bottom and a mass component, or proof mass, suspended by a flexible hinge on the top. The electrodes include a tip electrode, proof mass electrode, and deflection electrode. The metal of the electrode is a layer of Au film because of its inert chemical characteristics as well as its relatively high work function. When operating, the accelerometer maintains a constant tip-to-proof mass distance by applying an electro static feedback force on the proof mass. The cross section of the tunneling accelerometer is illustrated in Fig. 3-1. Usually, at this constant distance operation point, the distance between the tip and proof mass electrode is about 10 Å and the tunneling current is about 1.5 nA. More detailed descriptions about tunneling structures and operation principles can be found in Ref. [26][27][28][29]

3.3 Modeling

A MatLab Simulink Model Block Diagram is constructed according to the accelerometer function structures as shown in Fig. 3-2. The external acceleration Δa is applied on the proof mass and produces external force F_{ext} , which causes a displacement change, ΔX , between the tip and proof mass. In order to reduce mechanical noise induced by thermal fluctuations, the tunneling transducer always operates at vacuum environment. Because of this, air damping can be omitted here. At force balance there exists $F_{spring} = F_{acceleration}$, that is $K\Delta X = m\Delta a$, where m and K are the mass and stiffness of the

proof mass. The K/m ratio is very important because it is inversely proportional to the sensitivity $\Delta X/\Delta a$ and describes the proof mass natural frequency $\omega_n = \sqrt{K/m}$. The K value is mainly determined by the sensor's structure and size, which can be calculated either by mathematical methods for simple structure or by simulation methods aided by ANSYS or other Finite Element Analysis (FEA) software. It is easier to measure the natural frequency and we can always arbitrarily choose the mass of the proof mass to satisfy the need for the K/m ratio. Here the natural frequency is chosen as the input parameter for MatLab. In order to exhibit fast response time and large bandwidth, accelerometers require high natural frequencies. For better sensitivity and resolution performance, a small K/m ratio is needed. The most challenging task for a tunneling accelerometer design is to enhance the resolution while broadening the bandwidth.

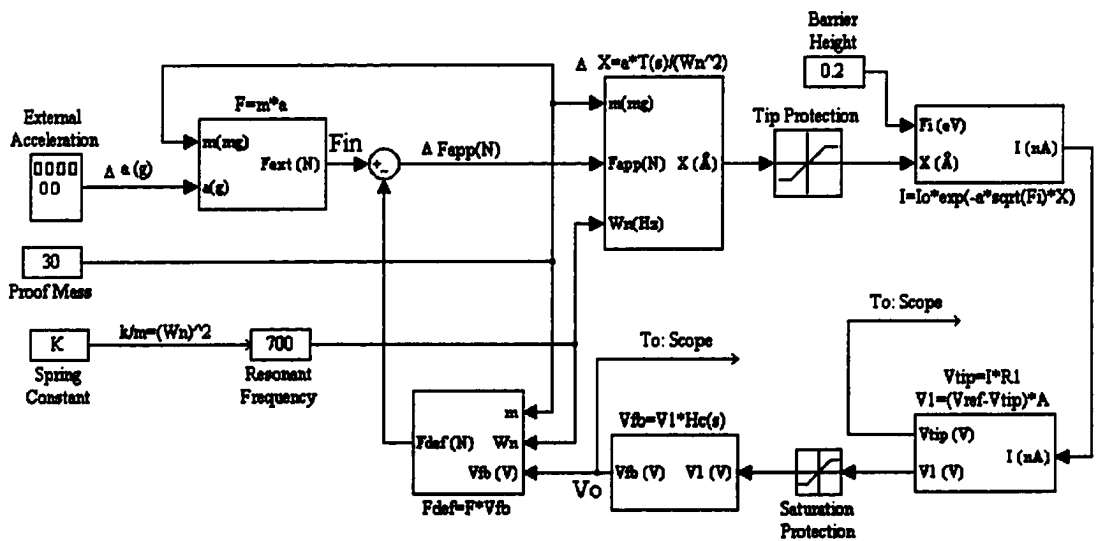


Figure 3-2 MatLab Simulink Modeling Block diagram

When a force is applied on a tunneling transducer, the distance change is

$\Delta X = \frac{a}{\omega_n^2} \cdot T(s)$, where $T(s)$ is the proof mass frequency response,

$T(s) = \frac{\omega_n^2}{s^2 + 2\omega_n\zeta \cdot s + \omega_n^2}$, with a second order model simulation. The relation between

damping ζ and quality factor Q is $\zeta \cdot Q = 1/2$. Because tunneling accelerometers are

flexible and they often operate under a vacuum environment, it is easy to obtain a large Q

value of 100 or more. Thus, the other purpose for control systems is to increase the

damping to get $Q_{eff} = 0.707$. The change between the tip and the proof mass, ΔX , induces

an exponential tunneling current $I = I_0 \exp(-\alpha\sqrt{\Phi}\Delta X)$, where α is a constant, $\alpha = 1.025$

($\text{\AA}^{-1}\text{eV}^{-0.5}$) and Φ is the effective height of the tunneling barrier, whose typical value is

0.2 eV. The tip voltage, V_{tip} , from the sample resistor, is compared with reference

voltage, V_{ref} , and amplified by a pre-amplifier thereafter. A control circuit with transfer

function H_c is followed and feedback voltage V_{fb} is produced. V_{fb} is input into an

electrostatic actuator, which produces a feedback force F_{def} . Usually the actuator is a

parallel capacitor whose force can be described as $F_{def} = \frac{\epsilon S (V_{hi} + V_{fb})^2}{2(D + \Delta X)^2}$, where V_{hi} is a

high DC voltage applied onto the actuator to set the operation point, D is the nominal gap

between the electrodes, ϵ is the permittivity, and S is the overlap area of the electrode

pads. F_{def} , in turn, counterbalances the external force and keeps the tunneling tip at the

operation point. The magnitude of feedback voltage V_{fb} is proportional to the external

force and is also called output voltage V_o .

3.4 Small Input Analysis

In the simulation model of a tunneling accelerometer, there are two non-linear blocks. One is the block between displacement changes and tunneling current, and the other is the block between the feedback voltage and deflection force. In order to synthesize the system, these two blocks are analyzed and linearized based on practical small signal input.

The changes of tunneling tip-proof mass distance, ΔX , is about $10^{-3} \sim 10^{-1}$ Å, which has been measured by laser vibration measurement system^[4]. ΔX is small compared with the normal operation position of 10 Å. The current can be developed by Taylor Series as $I = I_0(1 - a\sqrt{\Phi}\Delta X)$. Because sample resistor R_I is chosen such that the product of I_0R_I is equal to the reference voltage V_{rf} , it is easy to get $V_I = V_{rf} \cdot A \cdot a\sqrt{\Phi} \cdot \Delta X$, where A is the amplitude of the pre-amplifier.

For an actuator, the electrostatic force is proportional to $(V_{hi} + V_{fb})^2$, that is $V_{hi}^2(1 + \frac{V_{fb}}{V_{hi}})^2$. Because V_{hi} is a DC constant voltage, about 100V, and is much larger than V_{fb} , several milli-volts, the force can also be re-written as being proportional to $V_{hi}^2 + 2V_{hi}V_{fb}$. The first item is to set the operation point and the second item is what we are concerned with. That is to say the change of the deflection force is proportional to $V_{hi}V_{fb}$, more simply, $F_{def} = FV_{fb}$, where F is called feedback factor. The value of F can be either estimated or tested in a real actuator. An estimated value is 1.5×10^{-5} (N/V) with an overlap area of 0.2×0.2 mm², a high voltage of 160V, and a nominal distance of 2 μm.

With the above approximations, the non-linear system now can be treated as a linear system at wavelet analysis. If F_{ext} is the input variable and V_o is output variable, the open and closed loop transfer function is $H_o = H_c \cdot \frac{V_f A \alpha \sqrt{\Phi}}{m \omega_n^2} \cdot T(s)$ and $H = \frac{H_o}{1 + FH_o}$, respectively.

3.5 Feedback and Control Design

When considering accelerometer resolution, smaller natural frequency corresponds to a higher resolution. If the minimum resolved displacement is 10^{-2} Å, a 700 Hz proof mass should resolve $2 \mu\text{g}$ ($g = 9.8 \text{ ms}^{-2}$) acceleration. The natural frequency of a proof mass cannot be chosen larger if a μg resolution is wanted. The open loop property of tunneling accelerometers ceases to respond when the applied acceleration frequency is larger than the resonance frequency. The purpose for control system design is to keep a high sensitive and flexible tunneling proof mass while broadening the bandwidth. In addition, the transfer function, $T(s)$, is an unstable system. The control system needs to enhance the system stability so as to protect the tunneling tip against parameter disturbances and signal impulses. From the relation between H and H_o , the control circuit with transfer function H_c should be synthesized so that the system transfer function H satisfies:

- The bandwidth of the system should be larger than the interested signal bandwidth.
- The system should be a stable system.
- The system needs to have a small response time so as to respond quickly enough.

- The system damping should be optimized so as to get instant response and protect the tunneling tip.
- Within interested frequency bandwidth, the sensitivity should be linear.

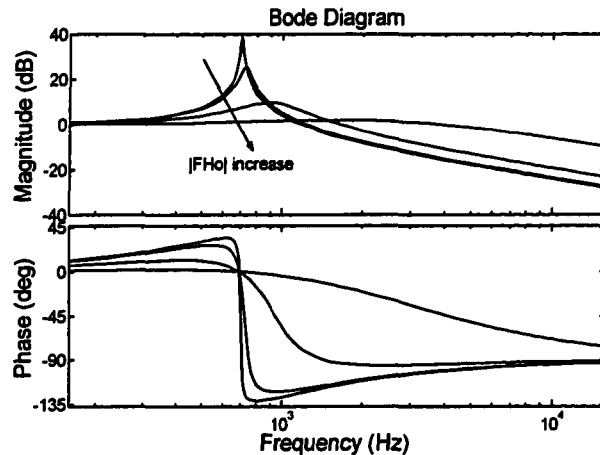


Figure 3-3 Normalized closed loop transfer function H' .

By feedback theory, the bandwidth and stability can be enhanced by a factor of $|FH_o|$. We hope to have $|FH_o| \gg 1$, which means a large open operation amplifier in the system is necessary. On the other hand, the system transfer function can be simplified as $H \cong 1/F$ in a deep negative feedback system. In order to have a higher sensitivity, we prefer a smaller F value. The strategy to lower F is to lower the DC bias voltage, V_{hi} . A large overlap area electrode and small nominal proof mass-deflection electrode distance are then often chosen. When starting to design, we first give a testing H_o , and then evaluate the closed loop transfer function H . If some conditions above are unsatisfied, we then change the controller H_c and give a correct testing H_o . All the synthesis processes are trial and evaluation. In fact, because of a large $|FH_o|$ value, it is not difficult to find proper control system functions to meet the design requirements.

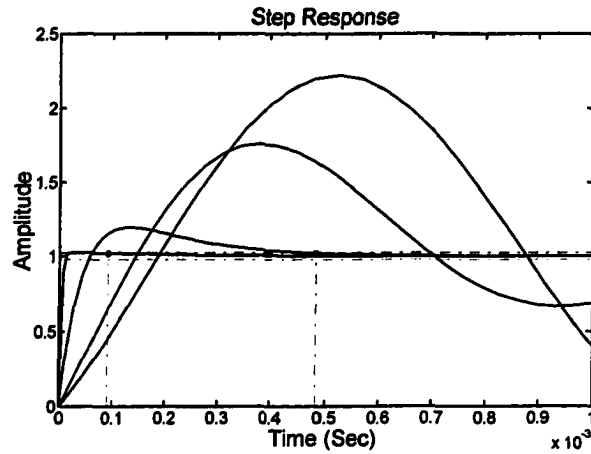


Figure 3-4 Step response of normalized closed loop system

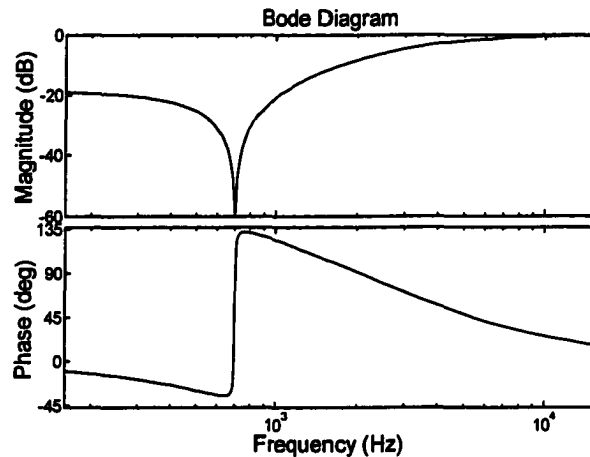


Figure 3-5 Bode diagram of synthesized control system

The changes of normalized closed loop transfer function H' dependent on $|FH_o|$ value are shown in Fig. 3-3. When the $|FH_o|$ value increases, the system stability also increases. The ultimate goal for us is to make a damping factor of a closed loop system $\zeta_{eff}=0.707$. A more detailed method of system damping chosen can be obtained from the step response of the normalized closed loop system. As shown in Fig. 3-4, a system with a settling time of 0.1 ms and an overshoot of less than 1% is marked. By choosing

feedback and a control system, the overall system can be both prompt to applied signals and stable with a proper damping ratio.

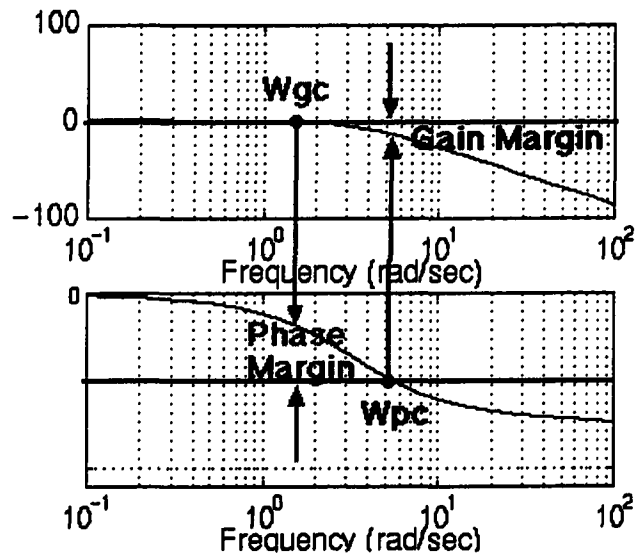


Figure 3-6 Gain Margin and Phase Margin illustration for control System

Without regarding that it represents a significantly better methodology, this method presents an easy alternative for new designs. Compared with the μ -synthesis method, our intended control system is not an exact and specific resolution for consideration. This relaxed requirement for the circuit is superior, though our designed control system is not as robust a controller as Liu's. However, as shown in Fig. 3-5, our control system has a similar property with this μ -synthesis controller.^[7] The very small low frequency sensitivity (-20dB) indicates the closed loop gain suffers minimally from open loop gain variation. At high frequencies, the applied signal gets phase compensation. At a bandwidth of 100Hz to 1 kHz, the overshoot and noise are suppressed.

3.6 Simulation Results and Discussions

3.6.1 Closed loop system evaluation

Gain & Phase Margin. The gain margin is defined as the change in open loop gain required making the system unstable. Systems with greater gain margins can withstand greater changes in system parameters before becoming unstable in closed loop. The phase margin is defined as the change in open loop required phase shift to make a closed loop system unstable. In bode plot, the phase margin is the difference in phase between the phase curve and -180 deg at the point corresponding to the frequency that gives us a gain of 0 dB (the gain cross over frequency, W_{gc}). Likewise, the gain margin is the difference between the magnitude curve and 0 dB at the point corresponding to the frequency that gives us a phase of -180 deg (the phase cross over frequency, W_{pc}), as shown below.

Figure 3-6 gives the gain and phase margin of the system. The gain margin is infinite and the phase margin is about 90 degrees, both of which are near the ideal value. The system is well stable.

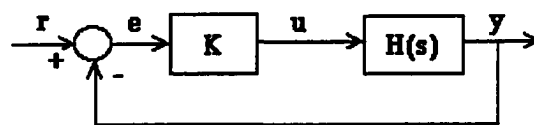


Figure 3-7 Illustration of root locus concept

Root Locus. The root locus of an (open-loop) transfer function $H(s)$ is a plot of the locations (locus) of all possible closed loop poles with proportional gain k and unity feedback (as shown in Figure 3-7).

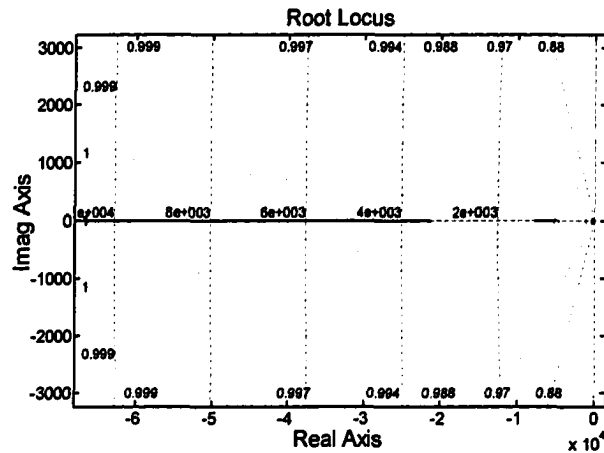


Figure 3-8 Root locus of closed loop system

The poles of the closed loop system are values of s such that $1 + KH(s) = 0$. We will consider all positive values of k . In the limit as k goes to 0, the poles of the closed-loop system are the poles of $H(s)$. In the limit as k goes to infinity, the poles of the closed-loop system are the zeros of $H(s)$. No matter what we pick k to be, the closed-loop system must always have n poles, where n is the number of poles of $H(s)$. The root locus must have n branches; each of them starts at a pole of $H(s)$ and goes to a zero of $H(s)$. Since the root locus is actually the locations of all possible closed loop poles, from the root locus we can select a gain such that our closed-loop system will perform the way we want. From the value of phase margin 90 degree, the damping is about $90/100=0.9$, which corresponding to an overshoot of approximately 1%. And the system will be close to being over damped. To determine what part of the locus is acceptable, we can plot a

line of constant damping ratio, as shown in Fig. 3-8. On the plot, the two white dotted lines at about a 45 degree angle indicate pole locations with damping of $\zeta=0.9$; in between these lines, the poles will have $\zeta > 0.9$ and outside of the lines $\zeta < 0.9$. In order to make the overshoot less than 1%, the poles have to be in between the two white dotted lines. All the poles in this location are in the left-half s-plane, so the closed-loop system will be stable.

3.6.2 Tunneling Accelerometer Function Simulation

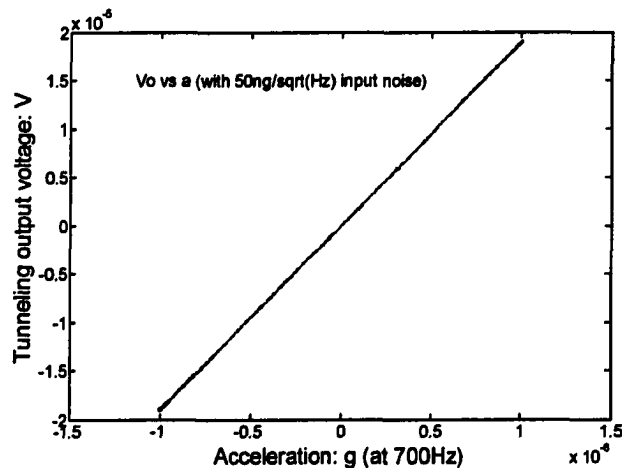


Figure 3-9 Transfer function of the tunneling accelerometer

The controller system is proved to have been successively synthesized from the evaluation of transfer function characteristics and system stability above. The functions of an accelerometer at an estimated noise environment are then simulated. A well-estimated thermo-mechanical noise level for tunneling sensor (equivalent as acceleration)

is $\sqrt{\frac{4K_B T \omega_n}{m_p Q}}$, where, K_B is Boltzmann constant; T is temperature; ω_n is resonant

frequency of the proof mass; m_p is proof mass and Q is mechanical quality factor. [30]
[31]

If we give Q as 50, the calculation value of the accelerometer noise is about 50 ng/\sqrt{Hz} . Fig. 3-9 is the plot of feedback voltage dependent on input acceleration. The linearity is kept until the input is out of the dynamic range, which is about 1.2 mg and it is well matched with the measured value. The small dynamic range is the price of high sensitivity because of the small k/m value. When horizontal signals are under consideration and the whole system is put in the horizontal direction, the small dynamic range would not cause problems in the earth's 1 g gravitational field.

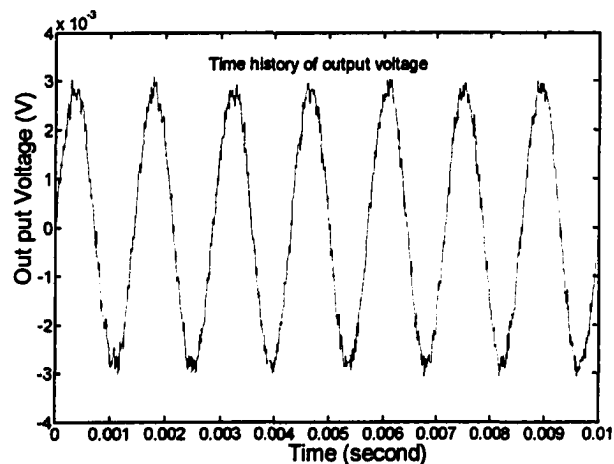


Figure 3-10 Time history of output voltage

Fig. 3-10 is the time history of accelerometer output at 700Hz when the input acceleration is 1.5 μg and the white noise level is 50 ng/\sqrt{Hz} . Fig. 3-11 is the semi log of current that depends on the bias deflection voltage to verify the tunneling effect. Without acceleration input and an open loop condition, the deflection voltage causes changes in tip current. The relation between semi log tunneling current and the deflection voltage fits

to the exponential tunneling equation very well and also can be used to measure tunnel barrier height, which is 0.2 eV as the MatLab Simulink designed. Finally, the sensitivity magnitude frequency responses of an open system and a closed loop system are plotted in Fig. 3-12. Though the sensitivity of closed loop is lowered at low frequency, the stability of the system is greatly enhanced and the sensitivity of voltage with respect to external force is about 95 dB up to 4 kHz.

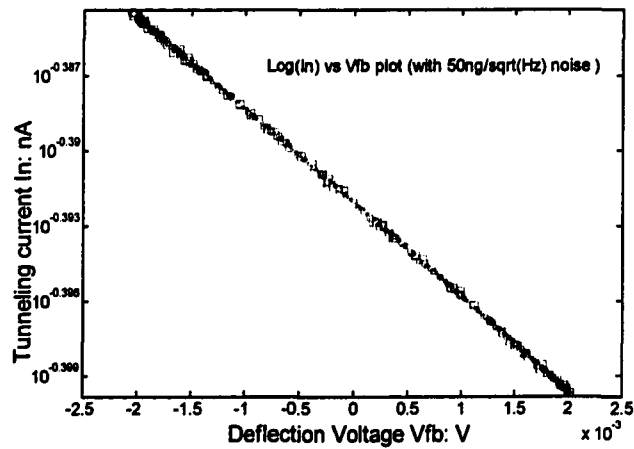


Figure 3-11 Tunneling current vs deflection voltage

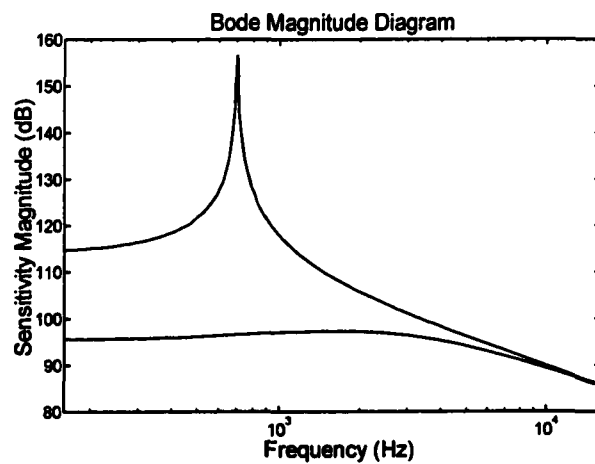


Figure 3-12 System sensitivity frequency responses

3.7 Summaries

In order to keep high sensitivity, the proof mass has a low resonant frequency and a high quality factor. On small input signal approximations, the tunneling accelerometer model is analyzed and linearized. The relationships of control systems, open loop systems, and closed loop systems are derived. Based on this approximation, a simple but effective means to synthesize a control system is successively exerted so that the closed loop system has broadened the bandwidth and optimized damping while maintaining its high sensitivity. The analysis of gain and phase margin, root locus, and pole distribution show the system is stable.

A model of a tunneling accelerometer sensor is constructed with MatLab Simulink. All the tunneling accelerometer functions, such as dynamic range, output voltage dependent input acceleration, exponential response of tunneling current, and frequency response of measurement are simulated and plotted.

CHAPTER 4

FABRICATION AND PROCESSES

4.1 PMMA Material Properties

The advantages of choosing PMMA substitute for silicon wafer to fabricate the tunneling sensor are its lower price, special mechanical properties and thermal characteristics. Here is a simple introduction about PMMA.

PMMA, (Polymethyl methacrylate), was originally used as a shatterproof replacement for glass. The barrier at an ice hockey rink, which protects fans from flying, is made of PMMA. The chemical company Rohm and Haas makes windows out of it and calls it Plexiglas. Ineos Acrylics also makes it and calls it Lucite. Lucite is used to make the surfaces of hot tubs, sinks, the ever-popular one-piece bathtub and shower units, among other things. PMMA is a transparent (>90% transmission), hard, stiff material with excellent UV stability, low water absorption and high abrasion resistance. It is very stable in high electrical fields (good track and arc resistance) and releases little smoke on combustion.

There is a great deal of interest in modeling PMMA molecular motions in condensed phases. However many of these motions take place over quite long time scales, while molecular dynamics are limited. This is because typically a time step of $1 \times$

10^{-15} s is used. Here is an illustration of the rotation of the ester- and alpha-methyl groups in poly (methyl methacrylate) (PMMA):

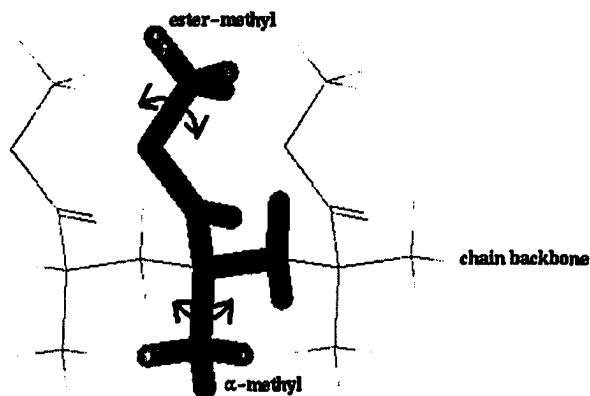


Figure 4-1 PMMA molecule and its rotation

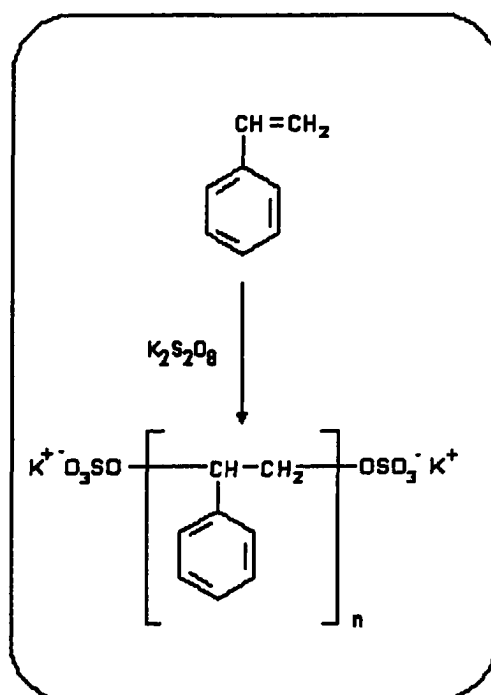


Figure 4-2 PMMA molecular structure

The ester-methyl group rotations in PMMA are fast, so this process can be modeled using dynamics as well. This enables a comparison between dynamics and

alternative (e.g. quasi-static) approaches to be made. Experimental data from Neutron Scattering are also available for this process.

Table 4-1. PMMA (Polymethyl methacrylate) at A Glance [32][33][34]

Physical Properties	
Uses	Thermoplastics
Monomer	methyl methacrylate
Polymerization	Free radical vinyl polymerization
Structure	Amorphous
Humidity absorption, 24hrs	0.3%
Density	1.18 g/cm ³
Linear Mold Shrinkage	0.004
Melt Flow; load 3.8kg	5.8 cm ³ /10min
Mechanical Properties	
Young's Modulus (E)	3.2GPa
Poisson's Ratio	0.43
Compression Strength	75.8~131 MPa
Tensile Strength	48~75.8 MPa
Tensile Modulus	2.4~3.4 GPa
Flexural Strength	82.7~117 MPa
Flexural Modulus	2.1~3.4 GPa
Impact Strength, Izod Notched	0.12 J/cm; 0.22 ft-lb/in
Gardner Impact	1.4J; 1.0 ft-lb
Hardness	R120; M80-M100
Stress at break	71MPa
Strain at break	3.5%
Thermal Properties	
Melting Point	112~130 °C
Glass Temperature	100~105 °C
Injection Molding, melt temperature	250 °C
Mold temperature	80°C
Deflection Temperature, 1.8MPa	90 °C
Max Operation (Service) Temp	80~93 °C
Vicat Softening Point	100 °C
Coefficient of thermal expansion, linear,	$7 \times 10^{-5} / ^\circ\text{C}$
Electrical Properties	
Dielectric constant; (100Hz/1MHz)	3.2/2.9
Dissipation Factor	0.04
Breakdown field	6×10^4 V/mm
Index of Refraction	1.48~1.5

A PMMA molecular structure is also plotted in Figure 4-2, which explains how the Unit can connect with other similar Units.

We checked the model of PMMA (G77) in I²M, and found the parameters of it as described in Table 4-1.

4.2 Fabrication of Mold

4.2.1 Photolithography

The purpose of photolithography is to transfer the pattern from glass masks, which are covered with Chrome films, onto SiO₂ coated Silicon wafer. Because the mold is the counter part of the sensor, the patterns should be transferred by negative photolithography when the pattern mask is clear field (The features are dark and the field is transparent). The negative photo resist used is NR9-1500. Here are the steps and explanation.

- The wafers must be clean and dry for good adhesion. The wafers need to be soaked in a solution of H₂SO₄ (98%) plus H₂O₂ with ratio of 7:3 at 70 °C for one or two hours. After being thoroughly rinsed, the wafers are baked on a hot plate for 30 minutes at 250 to 260 °C.
- When the dried wafers are cool, they are spun with NR9-1500 at a rate of 3000 rpm (revolutions per minute) for 40 seconds. Because of its large viscosity, the photo resist is thicker than positive photoresist, such as PR1813 or AZ1350. The thickness of NR9-1500 is 1.5 μm. The wafers are double spin so that the Silicon dioxide at back plane is also protected. The soft bake time is 4 minute for the back

side and 3 minutes for the front side. The bake temperature is about 130 °C. Only by soft bake can the photoresist become relatively hard and UV light sensitive.

- The soft baked wafers are loaded into an aligner. Due to the large critical dimension of about 30 μm , the exposure type is set as a close field exposure with a distance of 10 μm .
- The light is measured by a light intensity meter. The intended wavelength is 366 nm. The measured value is 188 mW/cm^2 . Because the total energy needed for NP9-1500 is 160~180 mJ/cm^2 , the exposure time is set as 10 seconds.
- At alignment, the pattern should keep parallel to the wafer's crystal line. A distorted pattern could cause inconvenience later.
- Post bake is necessary because the property of photo resist needs to be changed (the exposed part will change into polymer). The condition is not so strict here. It could be either 100 °C \times 120 sec or 115 °C \times 90 sec.
- After post bake, the wafers can be immersed directly into developer RD6. With a little agitation, the patterns appear at about 12 seconds. One or two seconds are needed for over development.
- After development, wafers are rinsed thoroughly. The wafers are blown dry and the patterns are checked under microscope.
- After photolithography, we still remedy the edge for post treatment. The purpose is to repair the defects made by tweezers scratches. A well-protected edge of wafer is necessary for BOE etching.

A photographic picture of a negatively patterned wafer is shown in Figure 4-3. The lines are straight and the strips are clear. If check under microscope, the pattern is perfect for wet etching.

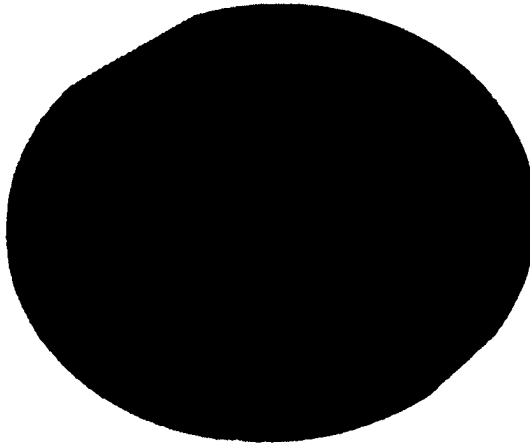


Figure 4-3 Patterned wafer by negative photolithography

4.2.2 BOE Etching

BOE (Buffered Oxide Etch) etching is the standard operating procedure for SiO_2 . Because HF solutions are considered both toxic and corrosive, uses of Trionic chemical gloves, safety glasses and a fume hood are required as a minimum. BOE is a very selective etchant, which means that it stops at the silicon and does not etch further. The etch may be used in many steps, such as exposing the active region near the beginning of a process or defining contact holes at the end.

BOE consists of HF acid at high concentration levels (about 10 times greater than the oxide strip in the RCA clean). HF acid is very dangerous and HF burns are particularly hazardous. An insidious aspect of HF burns is that there may not be any

discomfort until long after exposure. These burns are extremely serious and may result in tissue damage. If you contact HF, flush the area well and be sure to work under and around your fingernails. Fingernails and cuticles are the typical areas where people receive burns, having washed off the HF without washing under their nails. If washed off immediately after exposure, HF may do no harm. Also, immediately let the lab instructors know of any HF contact (immediately after flushing the area with water).

The Procedures of etching is as follows:

- Preparation of Solution - Will be done prior to each etching.

Chemicals include:

A. DI Water (DIH_2O)

B. Hydrofluoric Acid (HF)

C. Ammonium Fluoride (NH_4F)

- Here are the steps I followed in lab:

A. Mix 400 g of Ammonium Fluoride with 600 ml of water.

B. Carefully mix Ammonium Fluoride Solution with HF in a 6:1 ratio.

- The overall reaction for etching SiO_2 with BOE is:

$\text{SiO}_2 + 4\text{HF} \implies \text{SiF}_4 + 2\text{H}_2\text{O}$, where SiF_4 is solved into water.

- The buffering agent, ammonium fluoride (NH_4F), is added to maintain HF concentration and to control pH (to minimize photoresist attack).

The buffering reaction is:

$\text{NH}_4\text{F} \rightleftharpoons \text{NH}_3 + \text{HF}$.

- Etching Procedure are as follows

A. Mount wafer on Teflon wafer holder.

B. The etch rate for BOE is about 80 nm/min. An estimate of the appropriate etch time required is based on the known oxide thickness. There are two kinds of wafers are used, one covered with 1 μm oxide and the other with 2 μm oxide. The corresponding etching time are 13 min and 25 min, respectively.

C. Immerse wafer in BOE for the desired time. When complete, remove and rinse well with DI water, and blow dry with nitrogen.

D. If the etching was complete, then BOE and water should bead or "dewet" off the wafer because the silicon itself is hydrophobic.

E. After the etching is completed, inspect the wafers under the microscope. The etched regions with exposed silicon should appear to be silicon-colored (white or metallic-colored). If the exposed patterned regions still appeared colored, the wafers should be returned to the BOE.

F. Strip off the photoresist using oxygen plasma in the RIE. Alternatively, positive photoresist can be removed in acetone (possibly with ultrasonic agitation).

G. Using the Surface Profiler Meter to characterize the topography of the wafers to ensure that the etching was complete, especially when the condition of etching is not optimized at first experiments.

Figure 4-4 is the instrument of BOE etching. The Teflon holder is 4 inches in diameter with a rubber seal O ring. Tweezers are also plastic because metals are easily etched by the HF. The entire procedure is performed under a ventilated hood.

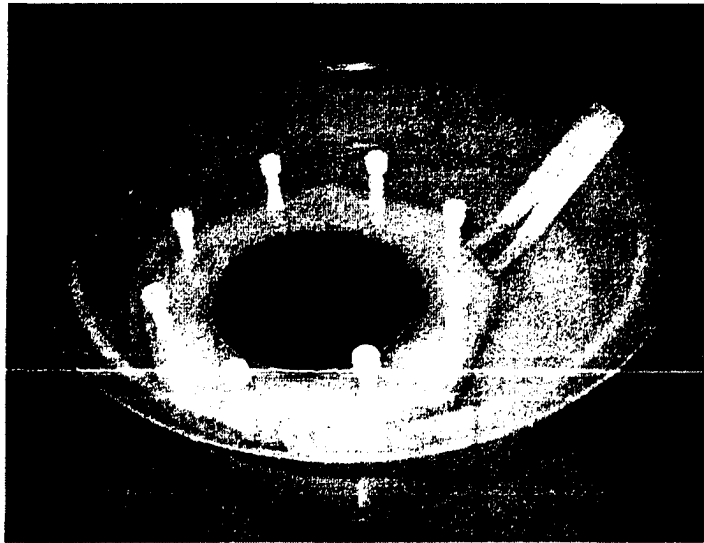


Figure 4-4 BOE etching of SiO_2

4.2.3 KOH Anisotropic Etching

Heated KOH solutions can be used for preferential etching of silicon along crystal planes. The etch rate will depend on the doping and crystal orientation of the silicon and the type of KOH solution used, but is typically on the order of about a micron per minute.[35] Potassium (K^+) is an extremely fast-diffusing alkali metal ion, and a lifetime killer for MOS devices. Thus, KOH etching is limited. Lab members using KOH must absolutely observe proper procedures to avoid contaminating any metal-ion sensitive processes and equipment elsewhere in the lab. KOH-etched substrates, however, may be later processed in "Clean" equipment, but only providing that the procedures for decontamination described here are strictly followed.

- Chemical Hazards

KOH solutions are caustic. The primary hazard classifications for KOH solutions are: Corrosive, air/water reactive. If you are using Isopropyl Alcohol in your KOH solution, remember that it is a solvent and that it is Flammable.

The 1:1:1 = H₂O:H₂O₂: HCl and 5:1:1 = H₂O:H₂O₂: HCl solutions are used for decontamination of wafers and tools following KOH etching. The primary hazard classifications for these solutions are: Corrosive, oxidizer, air/water reactive.

- **Process Hazards**

General process hazards involve handling of chemicals, and materials which come into contact with chemicals, used at this station. Wet benches are potentially the most dangerous operations in the lab. Be sure you understand all hazards and proper handling procedures before working at any wet bench. Be aware that KOH etching solutions and the H₂O:H₂O₂:HCl decontaminating solutions are heated, and not only present thermal hazards, but also chemical hazards that are more severe than what may be listed in the typical MSDS. (Material Safety Data Sheets)

- **Operation process of KOH Silicon Etching**

KOH Etching is done in the constant temperature. KOH decontamination may be performed with appropriately clean quartz containers or at silicide in the designated hot pot.

- **Etching with heated KOH**

A hot plate is used with temperature auto control by probe. By this way, the temperature can be reached within one hour and this set is more suitable for our little amount use. The typical instrument is shown in Figure 4-5. The rotation stir has a rotation

rate of 200 rounds per minute. The wafer is fixed by a Teflon holder. The lid of the beaker has been removed for the photograph. All the processing is fixed under the ventilated hood.

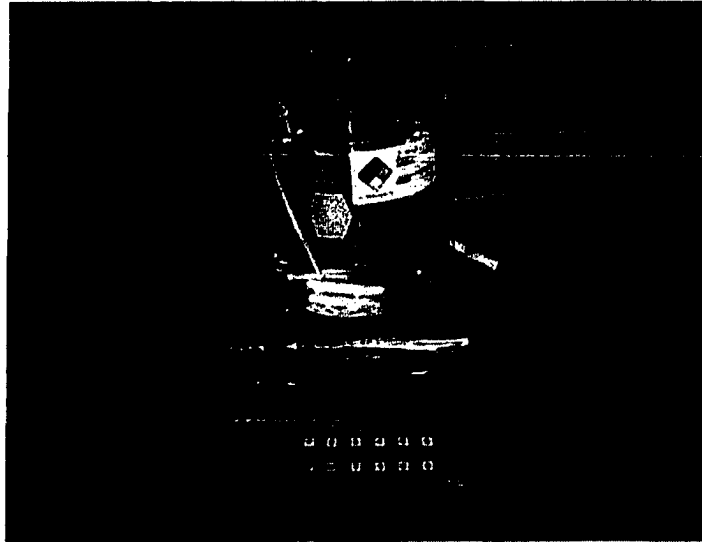


Figure 4-5 KOH etching process

- Information on KOH Etching of Silicon

Hot, concentrated solutions of KOH (and other alkali metal hydroxides) will etch along the (100) crystal plane several hundred times faster than along the (111) plane. KOH etching through mask openings $>1\text{mm}$ will result in a V-shaped pit that can go all the way through a (100) wafer of standard thickness.[36] MEMS engineers frequently design structures which exploit this etch preference, thus making KOH the most common method of machining silicon. Our window is $70\ \mu\text{m}$ in each side and the intended pit is pyramid like with a height of $50\ \mu\text{m}$ and base length of $70\ \mu\text{m}$.

Figure 4-6, 4-7 and 4-8 are illustrations of SEM pictures made when hot KOH etching. The cross section view shows the anisotropic etching angle is about 55° ; the SiO_2

mask layer is clear in the plot. The top views of the pyramid-like pit give us a clear view on what the mold like.

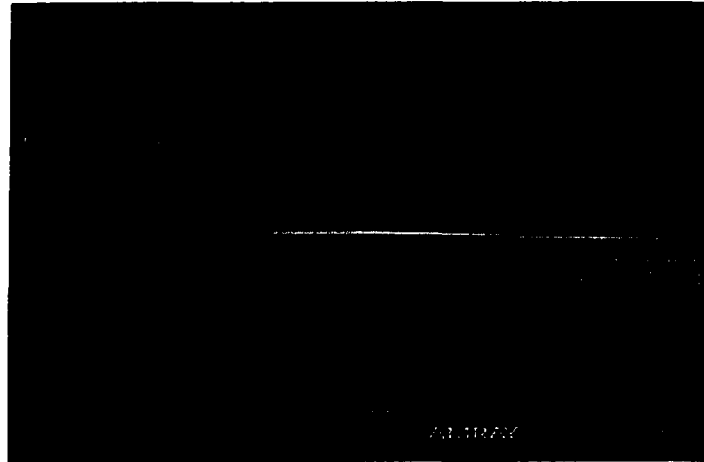


Figure 4-6 Cross section view of mold sidewall

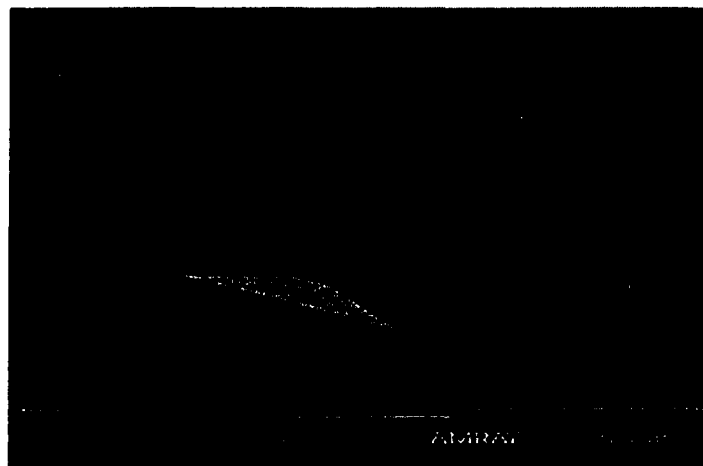


Figure 4-7 Top view of silicon window etched by hot KOH

Photoresist will not hold against the KOH etching. Silicon oxide can serve as a mask, although it still etches somewhere on the order of about 1 nm/min (oxide to silicon selectivity is a bit better in TMAH solutions). Silicon nitride is the preferred mask material (as little as 250 Å is sufficient for masking (100) etch all the way through a

wafer). For detailed process info, including references and recipes, consult Greg Kovacs' indispensable book, "Micromachined Transducers Sourcebook."



Figure 4-8 Top view of pyramid pit after hot KOH etching

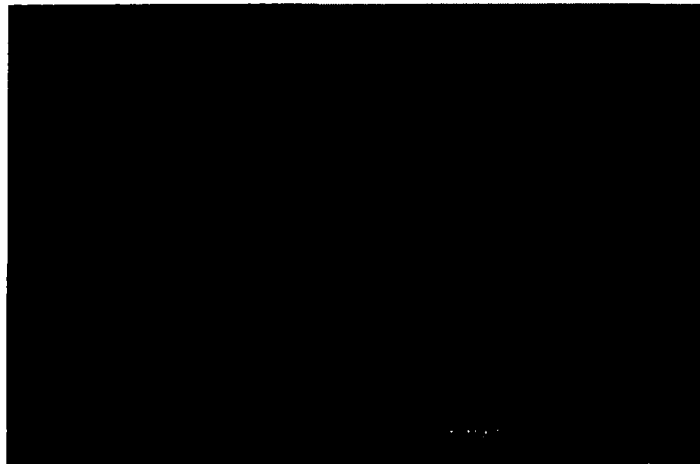


Figure 4-9 SEM plot of silicon mold made by hot KOH anisotropic etching

- **KOH etching of Silicon molds for hot embossing**

The molds for hot embossing have two kinds of structures. In order to simplify the processes, we designed two molds for different structures. The top mold includes proof mass and vibration sheet, and the bottom mold includes a tunneling tip and an

uphold bank. The most difficult thing is etching the pyramid-like pit, which has been shown in previous headlines.

The last masters for next processing should be clean, smooth, and precisely positioned. Clean molds can prevent the contamination of PMMA when hot embossed, which can not only destroy the PMMA structure, but is also harmful to the hot emboss system. A smooth surface is necessary because the demolding process needs the molds to be smooth enough for non-friction movement. The positions of structures are also important because the electrodes pattern needs to be exactly mounted on the right place. One photograph of such silicon wafer after hot KOH wet etching is shown in Figure 4-9. As shown in the plot, the mold is clean, smooth, and accurately mounted.

4.3 Hot Embossed Sensor Structure

With the development of LIGA technology [37][38][39] — X-ray Lithography, Electroforming (Galvanoformung) and molding (Abformung), three ways, electroforming, moulding, and embossing, to fabricate high aspect ratio structures have been attached more and more importance in Micro-electro-mechanical System (MEMS). As one of the most attractive micromaching techniques, hot embossing for replicating microstructures at a high performance-to-cost ratio has such advantages as: good uniformity, a surface roughness of only 3.9 nm at the large substrate area [40]; simple processing, needing only one step instead of multiple steps; and high resolution, a lateral resolution of only a few nanometers [41]. Moreover, by using inexpensive thermoplastic materials, such as polymethyl-methacrylate (PMMA) or polycarbonate (PC), the cost of the product can be further reduced. In addition, hot embossing itself consumes less

chemicals, takes less time, and needs fewer instruments than conventional semiconducting machinery. Therefore, hot embossing has been selected as one of the most popular tools for mass production.

In recent years, hot embossing has been used in many applications by exploiting the characteristics of thermoplastic materials. Because of such characteristics as insulating, biocompatible, and transparent, PMMA has been used in many applications like microfluidic channels [42], biotechnology patterns [43], and optical gratings [44][45]. In my research project, PMMA is specifically used in fabricating tunneling transducers because it is relatively softer than Silicon, which produces a potentiality in higher sensitivity.

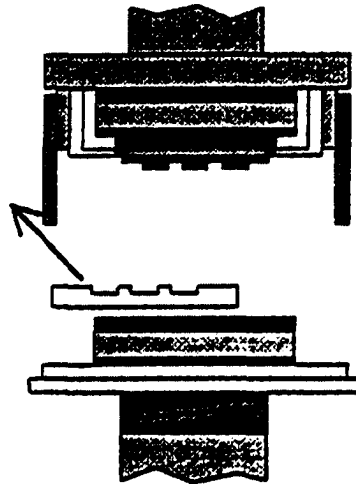


Figure 4-10 Hot Embossing illustration

4.3.1 Introduction About Hot Embossing

Hot embossing has its origins as the last step of the Lithographie, Galvanik und Abformung (LIGA) process, developed at the Karlsruhe Research Center, 'Abformung'

being the German term for 'replication'. [46][47][48] A polymer plate is laid onto the bottom heating plate of the embossing machine and the surrounding vacuum chamber is closed. Then, under vacuum, the heated mould insert is pressed into the softened polymer. After subsequent cooling, demolding takes place by removing the plastic part from the cavities. The microstructured part can be taken out of the machine. The processing is shown in Figure 4-10. Also, an embossing master and an embossed part in the machine are illustrated in Figure 4-11 and Figure 4-12, respectively.

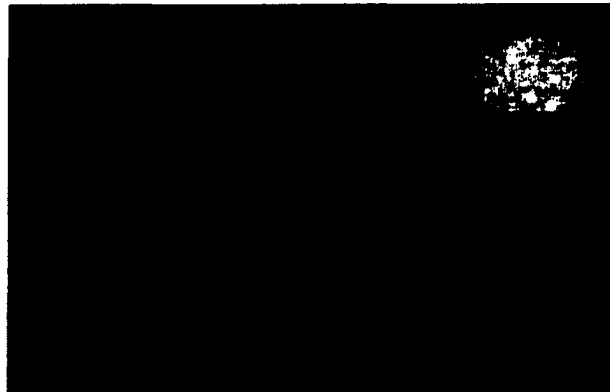


Figure 4-11 Hot embossing master



Figure 4-12 Photograph of embossed PMMA



Figure 4-13 Top part of hot embossing machine

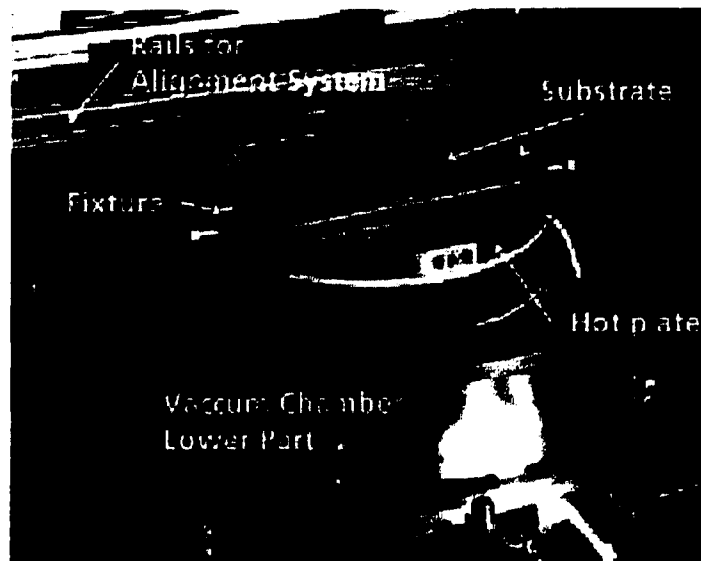


Figure 4-14 Bottom part of hot embossing machine

In hot embossing, high aspect ratio structures ($>10\text{mm}$) can be replicated quite easily, compared with injection moulding. It is possible to work with thin plastic sheets ($<0.5\text{ mm}$) in cases where a customer's needs restrict the thickness of the part. Due to rheological reasons, comparable injection-molded parts with a sufficient quality of the

microstructures need a minimum thickness of approximately two millimeters. For prototyping, hot embossing is far better suited than injection-molding, due to the easy mounting procedure and the fewer parameters required varying the replication process.

Recent progresses in machine technology have allowed reducing cycle-time in hot embossing significantly for certain polymers. Figure 4-13 illustrates a top part in hot embossing machine and Figure 4-14 is a bottom part in the machine.

4.3.2 Parameters and Properties

Our hot embossing machine is produced by JENOPTIC MIKROTECHNIK GMBH Inc., Germany. The range of embossing force is up to 50 kN and the process speed is controllable from 1 $\mu\text{m}/\text{min}$ to 8 mm/s. The main components include:

- Object system
 - Vacuum chamber, upper part
 - Upper non-parallelity correction
 - Demolding unit
 - Tool chuck
- Positioning unit
 - Lower non-parallelity correction
 - Sliding stage
 - Vacuum chamber, lower part
 - Substrate chuck
- Vacuum system
 - Pump

Ventilation

Vacuum measurement

- Temperature control unit

Heating/cooling

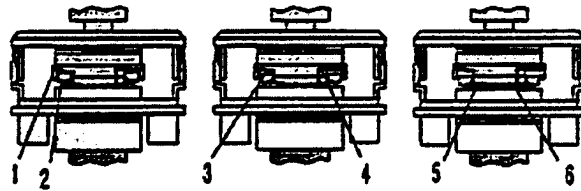
Temperature control of object system

- Electronics/software unit

Electronic cabinet

Software

The description of molding process is as follows. The central chamber part is movable. It has a square ring to seal it off against the stationary chamber part, and an O-ring which presses against the sliding plate at the chamber bottom. As analyzed in chapter 2, the glass temperature of PMMA is about 100 ~ 105 °C and melting temperature is about 112 ~ 130 °C. We set the molding temperature about 165 °C, which is a bit above the melting temperature, in case of uncertainty. When molding, the chamber is compressed down, and the maximum contact force is 18 kN. The background pressure is about 1.5 mbar. The master is held on for about 60 seconds and then the temperature is reduced. The demolding process is more important because all the parameters should be well controlled so that the microstructures are not destroyed by either cracking of the mold or friction against the side wall. The demolding system is designed to overcome the holding forces between tool and work piece material after molding. To achieve this, pressurized air is applied from the top. As shown in figure 4-15, the whole demolding process is in two steps:



- | | |
|-----------------------------|-----------------------------|
| 1. Port for seal pressure | 2. Pressure plate |
| 3. Volume for seal pressure | 4. Port for demold pressure |
| 5. Tool | 6. Substrate |

Figure 4-15 Schematic of demolding procedure

First step: the pressure plates are sealed off against the substrate (diagram in the middle of the Figure 4-15). The air is introduced through port 1 and it builds up pressure in volume (3) and causes the pressure plate (2) to act like a pneumatic cylinder, i.e., the plate moves down, sealing the chamber space against the substrate.

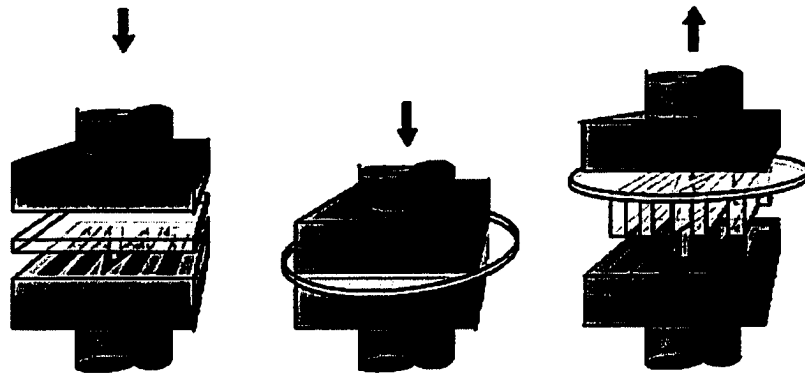


Figure 4-16 Flowchart of the hot embossing process

Second step: a demolding force is applied (right diagram in Figure 4-15) on the tool (5), the pressure plate (2) and the substrate, creating one common volume, which is filled with pressurized air via port 4. If the tool and the substrate move apart at low speed, the pressurized air will support the demolding in the substrate's marginal areas by force. As the apart motion continues, more and more parts of the substrate area become exposed

to pressurized air, until the substrate is completely demolded. In our case, the temperature is set as 80 °C when demolding. The speed of mold moving is 1 mm/min.

Table 4-2. Hot Embossing Commands and Explanation

Initial force control (true/false)=1;	basic force unit is initialized.
Temper (Top = 40 °C, Bott= 40 °C);	start heating of substrate and embossing tool
Close Chamber ();	close the vacuum chamber
Evacuate Chamber ();	evacuate the vacuum chamber
Wait (120 s);	wait, let the background vacuum stable
Touch Force (Force = 500 N);	tool and substrate move together till contact
Wait (60 s);	wait 60 seconds for system stable
Heating (Top=60 °C Bott= 90 °C);	start heating the tool and substrate slowly
Temper (temper>= 80 °C channel = 10);	system keep heating till 80 °C is reached
Wait time= 30 s;	wait until the temperature is stable
Heating (Top=60 °C, Bott =170 °C);	keep heating the tool and substrate
Temper (temper>= 160 °C);	heater continues until 160 °C is reached
Heating (Top= 60 °C, Bott=160 °C);	keep the tool and substrate temperature
Wait (30 s);	the function wait for 30 seconds
Force-Force controlled (Force =20kN, Vel = 1mm/min);	applies a force of 20kN for molding
Wait time (Time = 120 s);	system waits for 120 seconds
Cooling (Top = 60 °C Bott = 70 °C);	starts cooling the substrate
Wait (Time = 20 s);	wait the temperature cooling
Temper (temper<= 85 °C channel = 10);	system waits until a temperature of 85 °C
Demolding();	demolds tool and substrate
Venting ();	vents the chamber
Open chamber();	opens the chamber
Temp (Top = 30 °C, Bott = 30 °C);	sets the tool and substrate above room temperature, incase of moisture

The flow chart of hot embossing for a microstructure is illustrated in Figure 4-16[49]. The lists of command set in software are saved in macro-files. One typical

example for our PMMA hot embossing is plotted in table 4-2, with explanations at the right side.

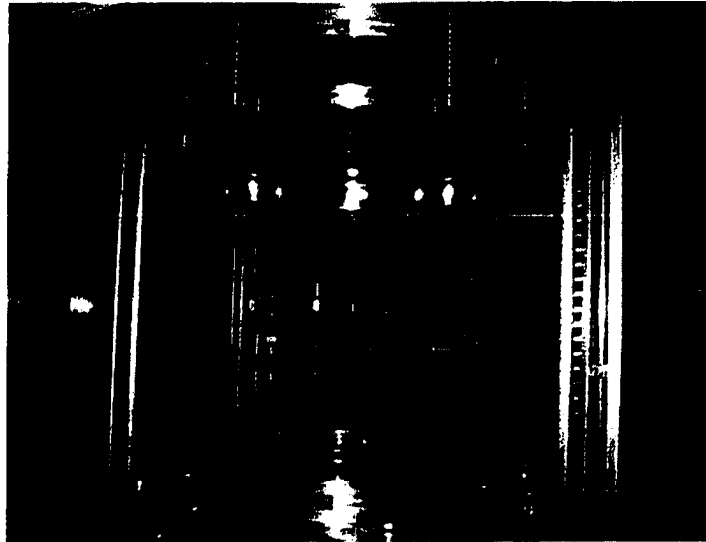


Figure 4-17 Hot Embossing machine overview

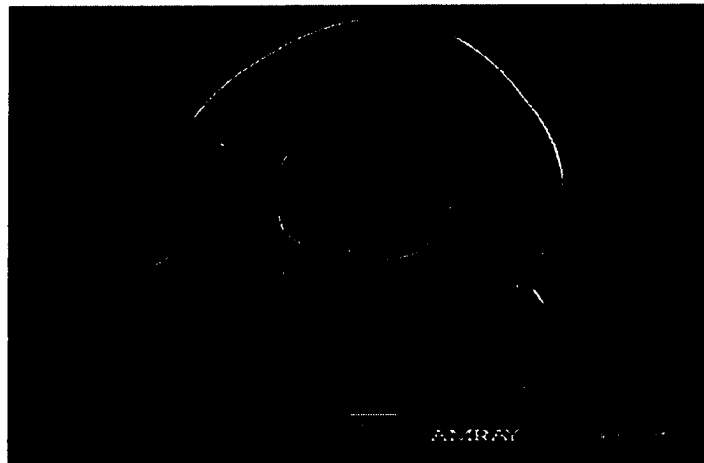


Figure 4-18 SEM plot of sensor right after hot embossing

The overall view of hot embossing machine is shown in Figure 4-17. A SEM picture of bottom sensor part is plotted at Figure 4-18. Compared with Silicon mold, the microstructure is totally transferred and without any defect. A close look of the tunneling

tip is shown in Figure 4-19. The tip is sharp and the edges are clear with a perfect pyramid structure. The tip height is about 50 μm , and each edge is about 70 μm .

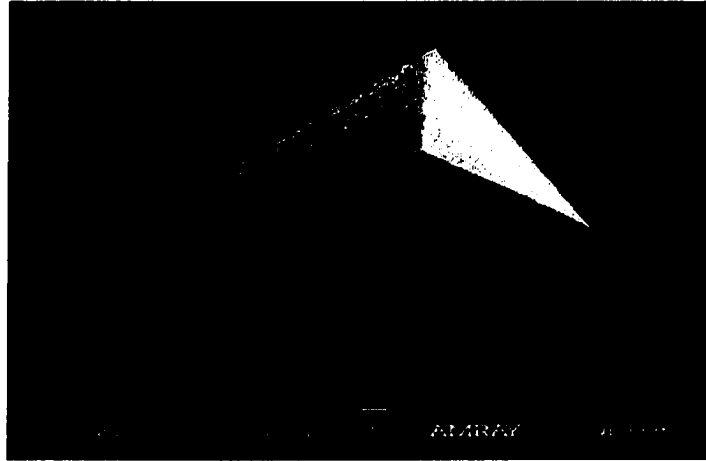


Figure 4-19 Close-up of tunneling tip made by hot embossing

4.4 Assembling and Packaging

4.4.1 Electrode Pattern

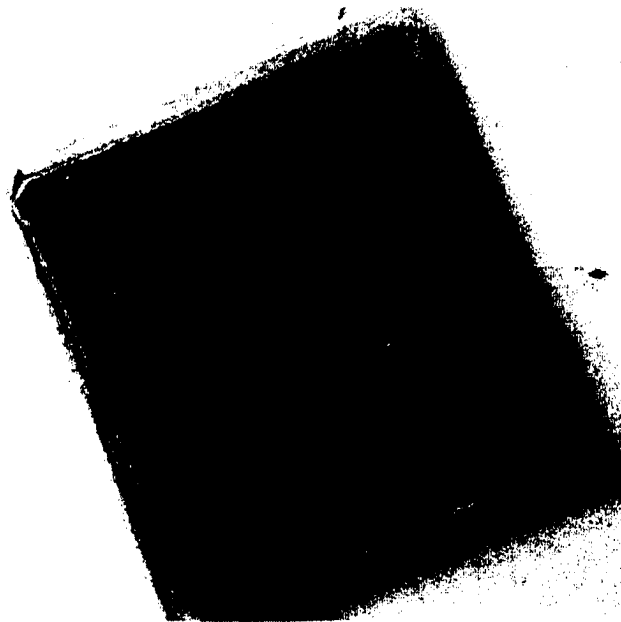


Figure 4-20 Photograph of patterned electrode

The metal film for electrodes is Gold because of its high work function as well as constant characteristics when current passing by the electrodes. In order to get better adhesion, there is a layer of Ti (titanium) film deposited before gold sputtering. The electrodes are patterned by positive photolithography with two steps of standard wet etchings. When etching Gold Electrode, we need to etch as follows:

- Au wet etching recipe (two kinds):

$I_2 + KI + H_2O = 10 \text{ kg} + 360 \text{ kg} + 1750 \text{ ml}$; etching rate: 100 Å/min

13 g KI (potassium iodide) + 7 g Iodine crystals + 250 cm³ water.

Our recipe is $I_2 : KI : H_2O = 1 : 5 : 50$ (weight), which produces an etching rate of 300 Å/min. After dissolving the KI in water, the solution may need to be heated to dissolve the iodine. This Au etch does not attack photoresist.



Figure 4-21 Close-up of electrodes

- Ti film etching

The most often used etching solution is BOE (Buffered Oxide Etch, usually used for etching SiO₂ on Si), which does not attack photoresist. BOE etches a 200 Angstroms Ti film within a few seconds.

After two steps of etching of Au and Ti, the PMMA sheets are well rinsed by DI water and dried by Nitrogen gas. A photograph of a patterned PMMA sample is shown in Figure 4-20, which has clear and golden areas for different parts. Figure 4-21 is the close-up of the central area, where a pyramid with gold coating is shown clearly.

4.4.2 Package

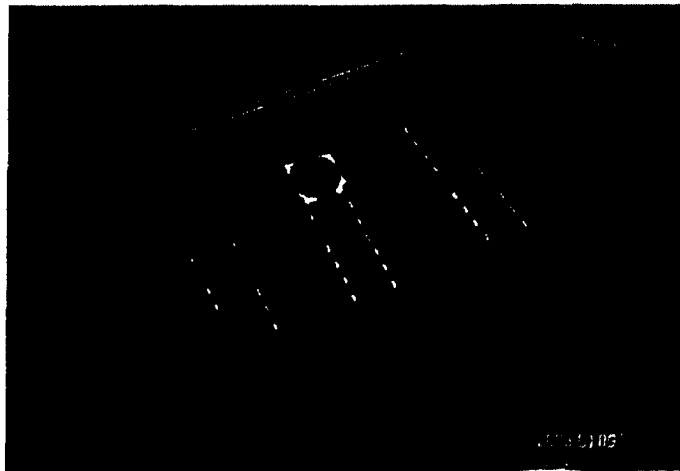


Figure 4-22 Packaged PMMA tunneling sensors

Our wire-electrode is not connected by wire bond but by electrical conductive glue. The model of our electrical conductive glue is Conductive Silver Epoxy Kit. This two-part silver epoxy is an electrically conductive silver filled epoxy adhesive recommended for a wide range of electronic bonding and sealing applications that require a combination of good mechanical and electrical properties. This two-part smooth paste formulation of refined pure silver and epoxy is free of solvents and copper or carbon additives. It develops strong bonds and coating between many different and dissimilar materials such as metals, ceramics, glass and plastic laminates. Two Part Silver Epoxy cures at room temperature and can be used as a "cold solder" for heat sensitive

components where hot soldering is impractical. It also can be used for the assembly and repair of electrical modules, printed circuit boards, wave guides, flat cable, and high frequency shields. This adhesive complies with the requirements of NASA's out gassing specification. There are also several important applications for the typical SEM laboratory. For example, this special silver filled epoxy is perfect for fastening down a sputter coater cathode to the head. And it is the ideal adhesive, when strength is really needed, for mounting a valuable or heavy sample onto a small (in comparison) SEM mount prior to analysis [50].

The two parts of our PMMA sensor are glued together also by the adhesive. Then it is fixed onto a 20-pin socket. The photographs of several packaged sensors are shown in figure 4-22.

CHAPTER 5

MEASUREMENTS AND DISCUSSIONS

5.1 Function Frame of Measurement System

The detailed measurement circuits are too complicated to get a clear overview. In order to explain the measurements in a concise way, the measurement system function frames are shown in Figure 5-1. In this figure, the measurement system is plotted as one negative feedback system while only the electrodes and connections are highlighted.

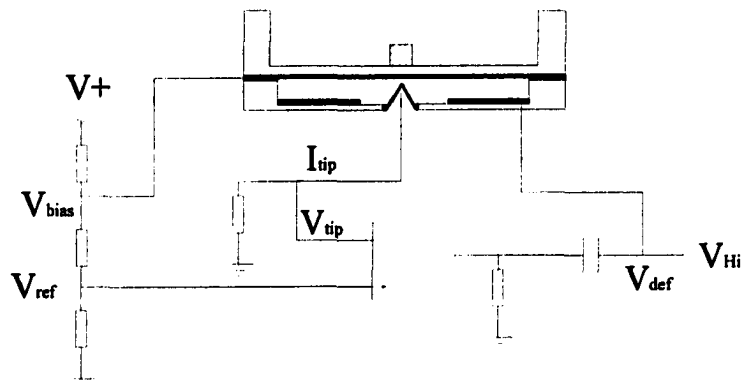


Figure 5-1 Function frames for measurement

The biased voltage is set as about 280 mV, which could produce about 1.5 nA when the tunneling tip is close to the counter electrode with about 10 Å, the counter electrode is pulled down by the high DC voltage V_{Hi} . The tunneling tip then produces about 30 mV through a 20 MΩ resistor. The reference voltage is also set at 30 mV so that

the output voltage is zero. When the applied acceleration (force) gives a small disturbance, the tip voltage will change, and then a negative feedback voltage is introduced to the deflection electrodes, which produces a force counter-balanced the applied force. In this way, a closed loop is set up. If we measure the feedback voltage, it should be proportional to the applied force. This is the mechanism of the tunneling accelerometer.

5.2 Resonance of Proof Mass

The measurement of resonant frequency does not need to connect the sensor with the circuits. This property is one of the mechanical characteristics. As shown in Figure 5-2, the packed tunneling sensor is glued onto the exciter. The vibration force is kept constant while the exciter's frequency changes. The induced vibration is measured by the laser vibrometer. The first resonant frequency produces a response peak at the response curve, which is also called natural frequency.

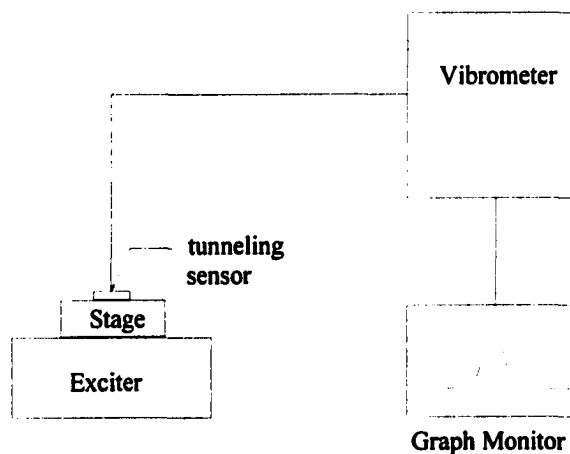


Figure 5-2 Resonant frequency measurement

The plot of measured data of the PMMA tunneling sensor is shown in Figure 5-3. The response is measured at an exciter of 1mg. The sharp peak corresponds to the natural frequency of $f_0 = 130$ Hz. Comparing with the simulated result of 150 Hz in chapter two, the difference is about 13.3%. The main reason should be the uncertainty of membrane thickness, which could range from 50 to 80 μm instead of a constant value of 50 μm .

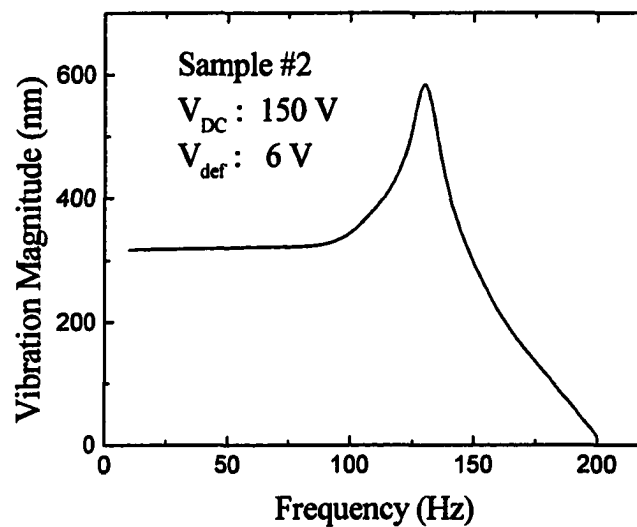


Figure 5-3 Measurement of natural frequency

5.3 Open Loop Measurement

Open loop disconnects both the reference signal and the tunneling tip with the amplifier input. As shown in Figure 5-4, the feed in signal now is the reference voltage, which is modulated by a frequency lower than natural frequency f_0 . The induced signals of deflection voltage and tunneling tip voltage have a relation if the high dc voltage is applied properly. When measuring, both of the deflection voltage and tip voltage should have the same frequency. The signals are all measured as effect value. The measured

curve of deflection voltage and tunneling voltage is plotted in Figure 5-5. From the curve, there is an exponential relationship between these two voltages. Later analyses provide proof of the tunneling effect.

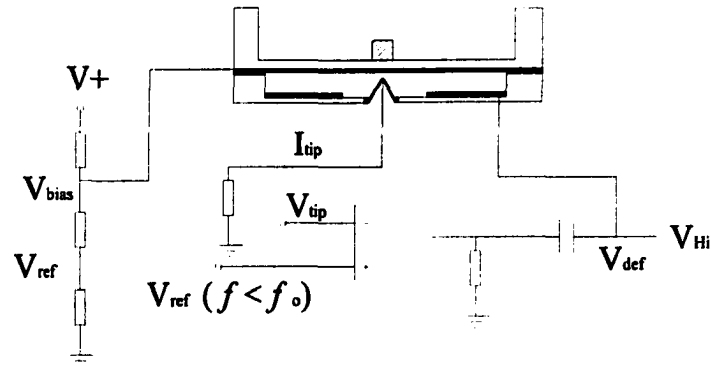


Figure 5-4 Open loop measurement

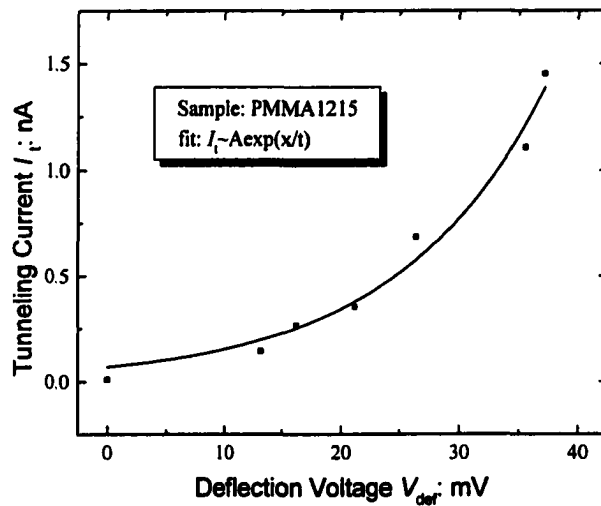


Figure 5-5 Tunneling current changes depend on deflection voltage

5.3.1 Electrode Deflection Rule

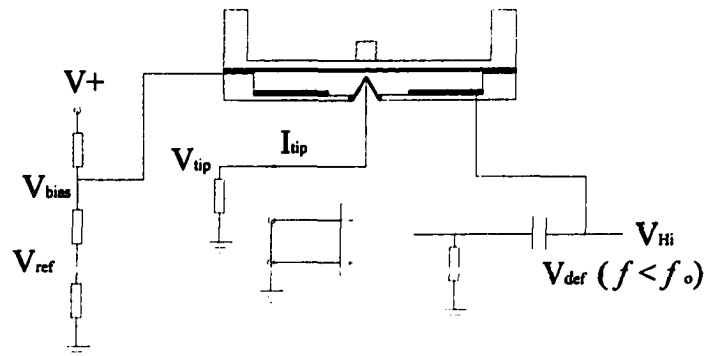


Figure 5-6 Actuator deflection rule measurement

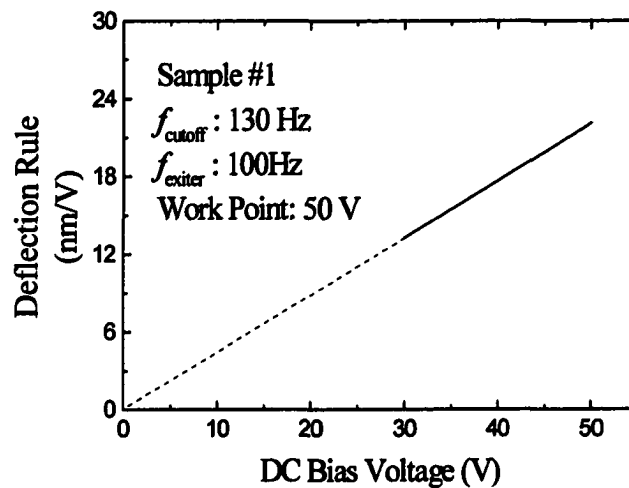


Figure 5-7 Deflection rule measurement

As the analyses in Chapter 2 and Chapter 3 indicate, the deflection voltage is linearly proportional to the tip movement because the capacitor actuator has a reciprocal square law between the gap and voltages. However, this relation must be measured before the sensor is quantified. The measurement is also at open loop status. As shown in Figure 5-6, the measure circuits are shortened with ground, which means there is no input signal into the circuits. Only a small ac voltage is directly applied to the deflection

electrodes. At the same time, the laser vibrometer is measuring the vibration amplitude when the deflection voltage is changing. The frequency of this deflection voltage should also be kept constant. This frequency is usually chosen as less than the natural frequency because there is no response for the mechanical system if not does so.

The measured curve is plotted in Figure 5-7, where the relation between deflection voltage and displacement movement is given out. The high dc voltage 50V is also given and should be written down because later on, we will use it.

5.3.2 Tunneling Current Verification

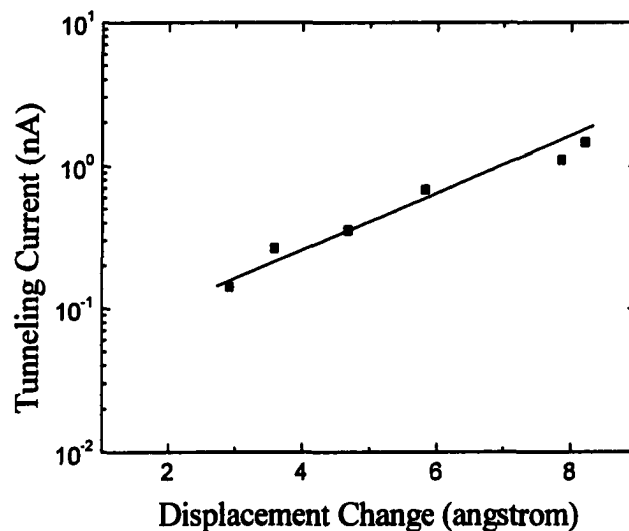


Figure 5-8 Tunneling relation between current and displacement

Derived from analysis above, the data of Figure 5-5 can be changed as the relation between the tunneling current and the movable tip-counter electrodes gap. This is the demonstration of the tunneling effect. The semilog plot is shown in Figure 5-8, where the

effective barrier height $\Phi = 0.1685$ eV is obtained according to the formula of $I \propto V \exp(-\alpha \sqrt{\Phi})$, which is rather similar with the values from other groups [25][29].

5.4 Closed loop Responses

The characteristics obtained above are the basic properties of tunneling sensors. In order to transfer the acceleration into voltage, the closed loop measurements are necessary. Here are the descriptions of the measurements.

5.4.1 Sensitivity

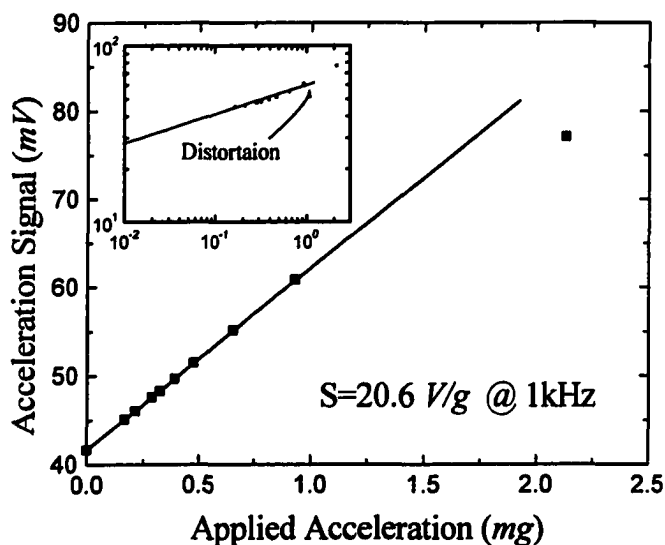


Figure 5-9 Sensitivity measurement of PMMA accelerometer

Sensitivity describes the property of the sensor's ability to transfer the acceleration to the measurable electrical signal. Here the output is the effective value of deflection electrodes. At a frequency lower than natural frequency, this transfer curve should keep a linear relation between acceleration and voltage. Figure 5-9 is the illustration of such a sensitivity measurement result. From the acquired data, the

sensitivity is 20.6 V/g ($1 \text{ g} = 9.8 \text{ ms}^{-2}$), which, however, can only be kept lower than 1.5 mg , where the linear relation is ruined (As shown in the insert picture of sensitivity log plot).

5.4.2 Frequency Response

The sensitivity is constant at the linear range of acceleration input when the exciter frequency is located at some area. The frequency characteristics are also important because they describe the possible work frequency range. The sensitivities at different frequencies are measured while the input accelerations are kept the same. There exists a cut off frequency at the sensitivity vs frequency curve, where there is no quick frequency response. The value of bandwidth, $B = 6.3 \text{ kHz}$, is plotted in Figure 10. It is no surprise that B is larger than natural frequency f_0 because the feedback system improved the stability, broadened the bandwidth and lessened the fluctuation, as described in chapter three.

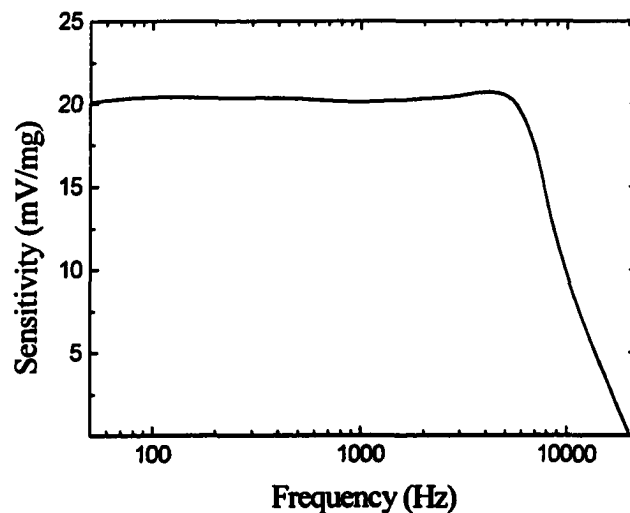


Figure 5-10 Bandwidth measurement of PMMA sensor

5.5 Resolution Measurement

Maybe the most important characteristic of sensors is their resolution, which describes the smallest signal one sensor can measure. Before the resolution measurement, we need to know what the noise is.

Noise, also known as white noise, is kind of signal that never repeats and has a flat frequency spectrum. Random noise is generally considered to have a Gaussian amplitude distribution, but numerically generated noise can also have a flat amplitude distribution. The amplitude of random noise is normally measured as the RMS value. In order to get a clear understanding of noise measurement, the basic concepts and fundamental equations related to noise are introduced below.

5.5.1 Noise

Noise, and its effect on electronic communication, is defined in many ways. There are many definitions of noise, such as white noise, pink noise, thermal noise, shot noise, equivalent noise, signal-to-noise, noise factor, and noise figure. Here, we will limit our investigation of noise to the following illustrations and equations.

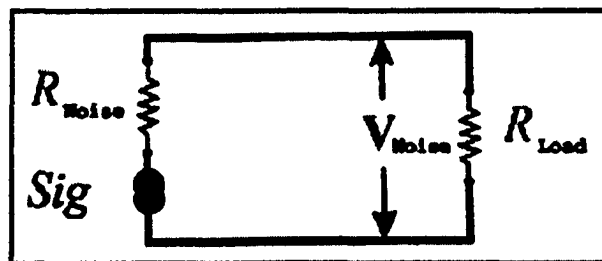


Figure 5-11 Elementary thermal Noise Generator

First, assume there is a circuit as shown in Figure 5-11. This schematic resembles a simplified representation of a base-band laboratory signal generator where the Sig is

assumed to be the signal output, which is noise free. However, the generator also has a noise output, and it is represented by R_{Noise} , the generator's internal resistance.

The noise power produced by a given, defined resistor noise source is approximately: $P_{\text{resist}} = P_N = kTB$; Where:

P_N = thermal noise power output of a resistor

k = Boltzmann constant, 1.38×10^{-23} joules/K

T = absolute temperature, Unit: K = 273 + C

B = system bandwidth

The noise voltage produced by R_{Noise} is approximately: $V_N = \sqrt{4kTBR}$, that is $V_N = \sqrt{4RP_N}$.

Although the relation between noise power and noise voltage is derived from thermal resist noise, it is also in effect at other places such as here, where an engineer unit instead of voltage is involved.

In most cases, the measured systems are more complicated. At least, there is an amplifier with gain S playing an important role between signal input and output. However, the real noise at output is something more “net” than original noise because the system has a bandwidth, which filters most of the noise at higher frequencies. Then the concept of spectral density is important.

Power Spectral Density (PSD) is used when measuring continuous broadband noise, and normalizes the power to an equivalent bandwidth of 1 Hz, irrespective of the actual bandwidth of the filter being used. That is to say, we need to transfer all the noise

power into power spectral density so that we can compare and use it to get the original signals.

There are many methods to measure a noise. Here, only two ways are used.

5.5.2 Time History Record

As shown in Figure 5-12, the tunneling sensor is put into a quiet environment, where there is no force or acceleration. The feed-ins are all set at zero, which produces zero thermal fluctuation noise from resistors. The deflection voltage, which now comes from noise, is recorded for a period of time and then analyzed.

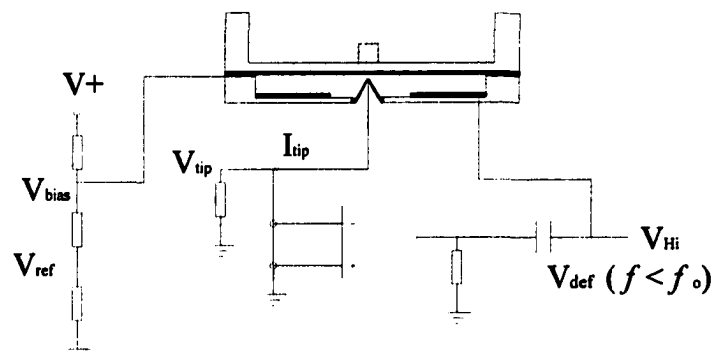


Figure 5-12 Noise measurement

If you are making an RMS measurement on a random noise signal, the error of the measurement will typically be dominated by the effective number of statistical averages performed, and not as much on the actual "sine wave" (data sheet) accuracy of the instrument. The random error (with 95% confidence which corresponds to 2 sigma (standard deviations)) of a measurement on random noise signals is equal to $\varepsilon = \frac{1}{2\sqrt{BT}}$;

where B = Bandwidth of the measurement in Hz; and T = the average time in seconds.

So, the measure time of 1 second is long enough to make sure the error is below 5% if the bandwidth is 100 Hz.

The recorded noise voltages V_{Nd} are peak to peak value. The RMS noise voltage is then equal to $V_N = \frac{V_{Nd}}{2\sqrt{2}}$. The Figure 5-13 gives the time history record of noise. After

being transferred to the input end, the noise level is: $\frac{V_N}{S} = \frac{\sqrt{(V_{Nd})^2 / 8B}}{S} = 0.232 \mu\text{g} / \sqrt{\text{Hz}}$,

which is in the same order as designed value.

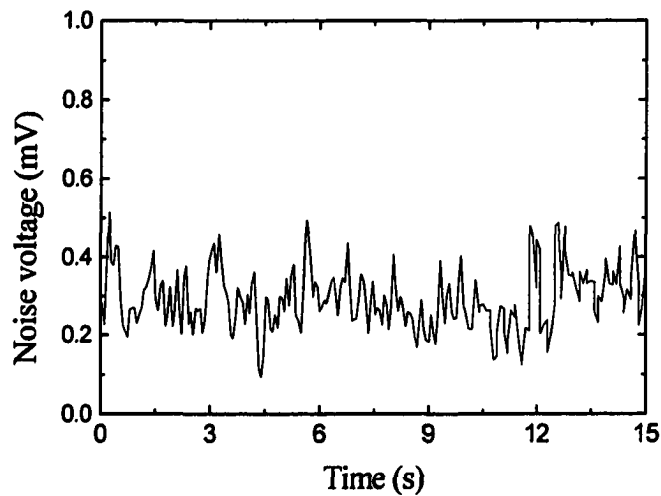


Figure 5-13 Time history record for 15 seconds

5.5.3 Noise Level Resolution

The second way to measure noise is to get the frequency spectrum of noise directly. The reason we are concerned more about the noise mechanism is that we are concerned about the distribution of the noise and the real reason of noise. Usually, the spectrum is measured on one block of data and no averaging is performed with FFT. The spectrum consists of a number of periodic components (one vector per frequency), which

are most often displayed as magnitude and phase information. Most instruments do not show the phase part. Normally, the magnitude is expressed in Volts (V) or power (V^2). When the FFT is used to calculate the Frequency Spectrum, the frequency components will have a linear spacing. For example, a 1000 points time block will be transformed into 500 frequency components that are equally spaced.

Figure 5-14 is the frequency spectrum of sensor noise. The noise behaves as white noise at the frequencies higher than 192 Hz. The white noise level is 405 μV . At lower frequencies, the noise increases quickly, which shows a $1/f$ behavior. The reason for noise origin is still an open question, though there are some concerns that the noise comes from the thermal fluctuation of environment.

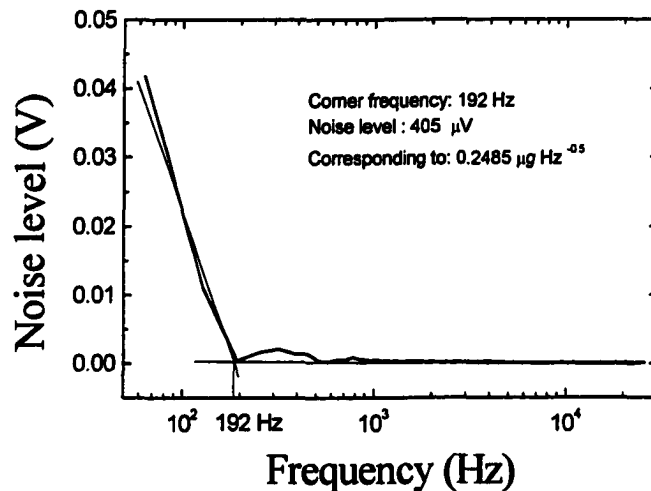


Figure 5-14 Noise spectrum of PMMA tunneling sensor

Again, the noise is transferred into the input end as:

$$N_a = \frac{V_N}{S} = \frac{\sqrt{(V_N)^2 / B}}{S} = 0.2485 \mu\text{g} / \sqrt{\text{Hz}} ; \text{ where } N_a \text{ is the acceleration resolution described in } g / \sqrt{\text{Hz}} .$$

CHAPTER 6

CONCLUSION AND FUTURE WORK

6.1 Conclusion

This project includes two parts. The first part is to use hot embossing technique to realize the PMMA micromachining. The second part is to fabricate vertical tunneling transducer with all-PMMA materials instead of the more conventional Silicon. With two years of hard work, these two purposes have been reached with the specifications below.

6.1.1 Structure Simulation by ANSYS

Just before the fabrication, the mechanical and possible structure data are simulated through all kinds of software. By ANSYS, the data were obtained before fabrication. The related properties are:

Static analysis: The structure deflects and bends at the static force application. The thickness of proof mass film should be about 50 μm . The force will not produce distortion within the tension limitation.

Model analysis: Four possible vibrations are simulated and the first frequency is obtained when damping is neglected. The other high vibrations could be avoided if the excitation of the system at a frequency lowers than natural frequency, which is the resonant frequency.

Harmonic response: The tension and steady response are analyzed when the proof mass parts are synthesized. The displacement response, when damping exists, is simulated and shown, which gives estimation how much the proof mass film is needed under static force.

Static force and bending: The actuator parameters are simulated according to the static force analysis. The distance of parallel capacitor actuator is about 20 to 50 μm , which set the height of the tunneling tip to range from 20 to 50 μm . The lateral sizes of the tunneling tip are then also set because of the relation angle of 55° with anisotropic etching.

Electrostatic actuator: The actuator parameters are also analyzed with the bend, applied ac voltage and high bias dc voltage on the deflection electrode. All possible values are included into the table 2-2.

6.1.2 Feedback and Control System Synthesis by MatLab

This is the first time the tunneling transducer has been linearized in a mathematical model. I have successfully used the Taylor series to linearize the tunneling current-gap relation and therefore make the entire closed loop system. With the aid of an actuator and feedback circuit, a simple but effective control system is obtained by CAD software of MatLab.

By choosing a feedback factor, the stability of the system is evaluated. From the gain margin and phase margin analysis, the open and closed loops of the system are all stable. The root locus illustration also shows all the unstable poles are in the stable district.

The tunneling accelerometer functions are also evaluated. The transfer function, which corresponds to the sensitivity of about 20 mV/mg , can only be kept within 1.2 mg . Both the sensitivity value and the dynamic range are quite similar to the measured value later. The time history record and output signal with noise have been simulated and predicted.

6.1.3 Combination Technique to Fabricate Silicon Mold for Hot Embossing

Both anisotropic KOH etching and plasma etching are used when Silicon masters are fabricated. The fabricated master has a smooth surface with positive profile, which is necessary when demolding. The pyramid silicon pit has sharp edges and a steep sidewall. The angle of 55° is automatically formed because of anisotropic wet etching.

6.1.4 All-PMMA Vertical Membrane Tunneling Structure Fabrication

An all-PMMA vertical membrane structured tunneling transducer has been successfully fabricated. The micro structures with pyramid tips in height of $50 \mu\text{m}$ possess smooth surface, steep edges and sharp angles. The proof mass blocks are also perfectly replicated from Silicon mold to PMMA.

6.1.5 Tunneling Effect Measurement and Evaluation

The exponential relation between the tunneling current and movable displacement proved that this tunneling transducer platform is highly sensitive and miniature. The measured resonant frequency is 130 Hz with about 400 nm in vibration magnitude. The sensitivity is about 20.6 mV/mg and restrains in linear area up to 1.5 mg . Then the

bandwidth of the closed loop is 6.3 kHz. Two kinds of noise measurement show the noise level is under $0.3 \mu\text{g} / \sqrt{\text{Hz}}$ with $1/f$ noise behaviors lower than 190 Hz.

6.1.6 Comparison with silicon-based tunneling sensor

The performances of a built PMMA-based tunneling sensor are better than or at the same order in magnitude as silicon-based tunneling sensor. A brief comparison of these two sensors is listed in Table 6-1. The data of silicon-based sensor are from one of the best groups until now at Stanford University.

Table 6-1. Brief comparison of PMMA- to silicon- based tunneling sensor

Properties	PMMA-based	Silicon-based
Natural response	133 Hz	100 Hz
Tunnel barrier height	0.1685 eV	0.212 eV
Actuator responsivity	400 nm/V	480 nv/V
Resolution	$0.2485 \mu\text{g} / \sqrt{\text{Hz}}$	$0.4 \mu\text{g} / \sqrt{\text{Hz}}$
Dynamic range	0-1.5 mg	0-1 mg
Sensitivity	26 V/g	44 V/g
Bandwidth	6.3 kHz	1.5 kHz

6.2 Future Work

This dissertation is just the first step for other applications based on all-PMMA tunneling transducer platform. There are two concerns right now.

6.2.1 Three-dimensional Accelerometer

The vertical PMMA sensor is objective to Z direction or one-dimensional sensors. However, three-dimensional sensors should be the ultimate purpose since the detected signal changes are unknown before measurement. Also, 3-D sensors can be widely used in industry environments.

The main idea is to integrate three identical sensors at three directions. Triple circuits are needed with similar output.

6.2.2 PMMA IR Sensor

The first application of an all-Silicon tunneling sensor was IR sensor, which has the exact same membrane structure as our PMMA platform. So it is convenient to directly use a PMMA structured IR sensor. Two membrane structured PMMA sheets are bonded together. The cavity with trapped gas, instead of proof mass this time, is sensitive to thermal radiation.

6.2.3 Chemical Sensor

Chemical sensors based on tunneling sensors can detect the changes of chemical density, mass, or other parameters when studying chemical reactions. This type of sensor is accomplished by the use of a membrane surface, which can detect the displacement amplitude changes produced by reactions. The small size of tunneling sensors enables many of them to be accurately inserted into a small volume of tissue or other specific place that is under investigation, a perfect situation for microsensors.

6.2.4 Magnetic Sensor

The PMMA-based tunneling sensor can meet the needs for low cost, low power and small, accurate sensors for civil, industry, military, and especially medical applications. The magnetic film, particle, and field properties then can be detected or inspected by the aid of this tunneling sensor. Cooperation with Louisiana State University for magnetic nano particle study has begun.

REFERENCE

- [1] J. L. Novak, IEEE International Conference on Robotics and Automation, May 14-19, 1989, pp. 137-144
- [2] D. H. Auston, IEEE journal of Quantum Electronics, 19, Apr. 1983, pp. 639-648
- [3] A. H. Bakker, and J. H. Huijsing, Proceedings of the 1995 21st European Solid-State Circuits Conference, IEEE Journal of Solid-State Circuits, 31, July 1996, pp. 933-937
- [4] I. R. Lauks, IEEE Transactions on Electron Devices, 26, Dec. 1979, pp. 1952-1959
- [5] T. Moriizumi, Proceedings of Transducers '95, the 8th International Conference on Solid-State Sensors and Actuators, 1 June 25-29, 1995, pp. 39-42
- [6] P. Gravesen, J. Branebjerg, and O. S. Sondergard Jensen, Journal of Micromechanics and Microengineering, 3, Sept. 1993, pp. 168-182
- [7] C. H. Ahn, and M. G. Allen, Journal of Micromechanics and Microengineering, 3, June 1993, pp. 37-44
- [8] C. F. Quate, et al., "Tunneling Accelerometer", Journal of Microscopy, 152, pp. 73-76, 1988
- [9] S. B. Waltman and W. J. Kaiser, "An electron tunneling sensor," Sensors Actuators, vol. 19, pp. 201-210, 1989
- [10] T. W. Kenny, S. B. Waltman, J. K. Reynolds, and W. J. Kaiser, "Micro-machined silicon tunneling sensor for motion detection," Appl. Phys. Lett. Vol. 58, pp. 100-102, 1991
- [11] P. Scheeper, J.K. Reynolds, T.W. Kenny, "Development of a model Analysis Accelerometer based on a Tunneling Displacement Transducer", Proceedings, Trransducer'97.
- [12] R. L. Kubena, G. M. Atkinson, W. P. Robinson, F. P. Stration, "A New Miniaturized Surface Micromachined Tunneling Accelerometer" IEEE Electron Device Letters 17, p. 306, 1996.
- [13] C. Yeh and K. Najafi, "A low-voltage bulk-silicon tunneling based accelerometer", 1996 Int. Electron Device Meeting Digest, P.23.1.1, 1996
- [14] "A novel infrared detector based on tunneling displacement transducer", Appl. Phys. Lett., vol. 59, pp. 1820-1822, 1991.
- [15] K. D. Muller, W. Bacher, M. Hecke, Process dings IEEE, MEMS 98, 263-267

- [16] K. Feit, K. D. Muller, M. Hecke, Micromat '99, Munich
- [17] C. Liu, A. M. Barzilai, J. K. Reynolds, A. Partridge and H. K. Rockstad, *Joun. of Microelectromechanical systems*, pp. 235, Vol. 7, No.2, June, 1998.
- [18] H. K. Rockstad, K. Reynolds and W. J. Kaiser, *Sensors and Actuators A*, 43 (1994) 107-114.
- [19] J. Grade, A. Barzilai, J. K. Reynolds, C. Liu, *IEEE TRANSDUCERS'97*, pp.871, Chicago, 1997.
- [20] S. B. Waltman and W. J. Kaiser, "An electron tunneling sensor," *Sensors Actuators*, vol. 19, pp. 201-210, 1989
- [21] C. H. Liu, J. D. Grade, A. M. Barzilai, J. K. Reynolds, A. Partridge, H. K. Rockstad, and T. W. Kenny, "Characterization of a High-sensitivity micromachined tunneling accelerometer", *Transducers'97*, pp. 471-472, International conference on Solid-State Sensors and Actuators, Chicago, June, 16-19, 1997
- [22] P. G. Hartwell, F. M. Bertsch, S. A. Miller, K. L. Turner, and N. C. MacDonald, "Single mask lateral tunneling accelerometer," in *Proc. IEEE Micro Electro Mechanical Systems Workshop (MEMS'98)*, pp. 340-344, 1998
- [23] John Grade, Aaron Barzilai, J. Kruth Reynolds, Cheng-Hsien Liu, Aaron Partridge, L. M. Miller, J. A. Podosek, Tom Kenny, "Low Frequency Drift in Tunneling Sensors", *Transducers'97*, pp. 871-874, International conference on Solid-State Sensors and Actuators, Chicago, June, 16-19, 1997
- [24] C. H. Liu, H. K. Rockstad, and T. W. Kenny, "Robust controller de-sign via μ -synthesis for high-performance micromachined tunneling accelerometers," in *Proc. 1999 American Control Conference*, pp. 247-252, 1999
- [25] Cheng-Hsien Liu and Thomas W. Kenny, "A high-Precision, Wide-Bandwidth Micromachined Tunneling Accelerometer", *Journal of microelectromechanical Systems*, vol. 10, No3, Sept. pp. 425-433, 2001
- [26] C. Yeh and K. Najafi, "CMOS interface circuitry for a low-voltage micromachined tunneling accelerometer," *J. Microelectromech. Syst.*, vol. 7, pp. 6-15, Mar. 1998.
- [27] J. Wang, B. McClelland, P. M. Zavracky, F. Hartley, and B. Dolgin, "De-sign, fabrication and measurement of a tunneling tip accelerometer," in *Proc. Solid-State Sensor and Actuator Workshop*, Hilton Head, SC, pp. 68-71 1996
- [28] R. L. Kubena, G. M. Atkinson, W. P. Robinson, and F. P. Stratton, "A new miniaturized surface micromachined tunneling accelerometer," *IEEE Electron Device Lett.*, vol. 17, pp. 306-308, June 1996.
- [29] Cheng-Hsien Liu, Aaron M. Barzilai, Joseph Kurth Reynolds, Aaron partridge, Thomas W. Kenny, John D. Garde, and Howard K. Rockstad, "Characterization of a High-Sensitivity

- Micromachined Tunneling Accelerometer with Micro-g Resolution”, *Journal of microelectromechanical Systems*, vol. 7, No. 2, pp. 235-244, June 1998
- [30] H. K. Rockstad, T. k. Tang, J. K. Reynolds, T. W. Kenny, W. J. Kaiser, and T. B. Gabrielson, “A miniature, high-sensitivity, electron tunneling accelerometer,” *Sensors Actuators A*, vol. 53, pp. 227, 1996.
- [31] C. H. Liu, J. K. Reynolds, A. Partridge, J. D. Grade, A. M. Barzilai, T. W. Kenny, and H. K. Rockstad, “A high-sensitivity micromachined accelerometer based on electron tunneling transducers”, in *Proc. ASME Winter Conference_Wymposium on Micro-Electron Mechanical systems*, Dallas, TX, pp. 13-20, 1997
- [32] Hung, et. al., “Further Analytical Study of Hybrid Rocket Combustion”, NASI-10210, 1972.
- [33] Karabeyoglu, et. al., “Transient Combustion in Hybrid Rockets,” AIAA 95-2691, 1995.
- [34] Wooldridge, et. at., “Internal Ballistic Considerations in Hybrid Rocket Design,” *J. Spacecraft*, Feb. 1967.
- [35] A. Horn, H. Schröder, E. Obermeier and G. Wachutka, “Simulation of Orientation-Dependent Etching of Silicon Using a New Step Flow Model of 3D Structuring”, *Proc. of 3rd Int. Conf. on Modeling and Simulation of Microsystems, Sensors and Actuators (MSM-2000)*; San Diego, CA, USA, 2000, pp 63-66.
- [36] H. Schröder, E. Obermeier, A. Horn and G. Wachutka, “Convex Corner Undercutting of {100} Silicon in Anisotropic KOH Etching: The New Step- Flow Model of 3-D Structuring and First Simulation Results”, *Journal of Microelectromechanical Systems*, Vol 10 (2001), pp 88-97.
- [37] E.W. Becker, W. Ehrfeld, P. Hagmann, A. Maner, D. Munchmeyer, “Fabrication of microstructures with high aspect ratios and great structural heights by synchrotron radiation lithography, galvanofornung and plastic moulding (LIGA process),” *Microelectron. Engng.* 4, 35-36, 1986.
- [38] J. M. Hruby, et al, “LIGA: Metals, Plastics, and Ceramics,” *Micromachining and Microfabrication Process Technology V*, Proceedings of SPIE, September 2-22, 1999, Santa Clara, CA.
- [39] J. Gottert, H. O. Moser, F. J. Pantenburg, V. Saile, and R. Steininger, “ANKA- a synchrotron light source for x-ray based micromachining,” *Microsystems Technologies*, Volume 6, Number 3, February 2000, pp. 113-116.
- [40] L. Lin, Y. T. Cheng, C. J. Chiu, *Microsystem Technologies* 4 (1998) 113–116
- [41] S.Y. Chou, P. R. Krauss, *Microelectronic Eng.* 35 (1997) 237-241
- [42] Marc J. Madou, L. James Lee, Kurt W. Koelling, Sylvia Daunert, Siyi Lai, Chee Guan Koh, Yi-je Juang, Liyong Yu, and Yumin Lu, *DESIGN AND FABRICATION OF POLYMER MICROFLUIDIC PLATFORMS FOR BIOMEDICAL APPLICATIONS*, ANTEC 2534-2538 (2001)

- [43] Schiff, H., Heyderman, L.J., Padeste, C. and Gobrecht, J.: "Chemical nano-patterning using hot embossing lithography", *Microelectronic Eng.* 61-62, 423-428 (2002).
- [44] N. Keil , H.H. Yao ,C. Zawadzki, Athermal polarisation-independent arrayed- waveguide grating (AWG) multiplexer using an all-polymer approach, *Volume 73, Issue 5-6*, pp 619-622
- [45] T. Ammer. M. Rossi, and M. T. Gale, "On-chip replication of micro-optical structures for VCSEL to fiber coupling", in *Proc. SPIE Vol. 440 (2001) 238*.
- [46] A Both, W Bacher, M Heckeke, K-D Müller, R Ruprecht and M Strohrmann (1996), *Microsystem Technologies 2*, pp. 104–108.
- [47] M Heckeke and W Bacher (1996), *Proceedings, 3rd Congress & 1st Europe-Asia Congress on Mechatronics, Besancon*, pp. 501–505.
- [48] L Weber, W Ehrfeld, H Freimuth and M Lacher, H Lehr and B Pech, *Micromachining and Microfabrication Process, Technology II, SPIE Proceedings Series, Vol. 2,879, Austin, 1996*.
- [49] http://www.fzk.de/imt/bereiche/fe2/e_inhalt_abformung.html
- [50] http://www.2spi.com/catalog/spec_prep/cond2.html